

1

Introductory NMR Concepts

1.1 Historical Aspects

Several reviews discussing the historic evolution of nuclear magnetic resonance (NMR) spectroscopy have been published (see, for instance, Emsley and Feeney (1995)), but the most comprehensive analysis can be found in various articles of the “Encyclopedia of Nuclear Magnetic Resonance,” edited by Wiley (see, for instance, Becker and Fisk (2007)). Here, we only highlight a very short outline of the most important developments, with a particular focus on the field of solid-state NMR (SSNMR).

The discovery of NMR can be attributed to Isidor I. Rabi (Nobel Prize in physics in 1944) and coworkers, who performed in 1938 the very first NMR experiment on a molecular beam of LiCl (Rabi et al. 1938). However, the first successful NMR experiments on solids and liquids were reported in early 1946 by two independent research groups at Stanford (Bloch, Hansen, Packard) and Harvard (Purcell, Torrey, Pound). Actually, the Harvard group led by Edward M. Purcell at MIT submitted a letter about their discovery to Physical Review on 24 December 1945, more than one month before the submission by the Stanford group to the same journal. However, it was established that the two researches were conducted independently and, for this reason, the 1952 Nobel Prize in Physics was awarded jointly to Bloch and Purcell. In particular, the group at Harvard discovered the phenomenon by studying solid paraffin in their very first experiment, and therefore, we can really say that solids were studied since the beginning of NMR.

The different behaviors between liquids and solids, as well as the anisotropic character of the nuclear interactions, were soon discovered by Bloembergen, Purcell, and Pound working on a CaF₂ crystal (Purcell et al. 1946). This was later explained in more detail by Purcell’s doctoral student, George Pake, who, through his studies on di-hydrated CaSO₄ crystals, first found the resonance signal that was a doublet and the typical pattern, now carrying his name, given by the homonuclear dipolar coupling between the two water protons in the case of single-crystal and powder samples, respectively. In the very first years of its life, NMR was mostly applied to solids and its study was rooted firmly in the physics community, for instance, to investigate molecular motions as a function of temperature from changes in a lineshape.

In 1950, Proctor and Yu (1950a, 1950b) fortuitously discovered chemical shift, i.e. how the local chemical environment surrounding a nucleus influences the frequency at which it resonates, by looking at the ^{14}N spectrum of NH_4NO_3 in water, and spin–spin indirect coupling, observing the ^{121}Sb resonance of NaSbF_6 in solution. Implications in NMR spectra became apparent, and most of the efforts moved to the study of liquids, characterized by much narrower lines. In the 1950s, tremendous strides were made in the development of the instrumentation. In 1952, the first high-resolution commercial spectrometer, working at a proton Larmor frequency of 30 MHz, was introduced by Varian and sold to Exxon in Baytown, TX, and at the end of the 1950s, a 60 MHz spectrometer was available. Great improvements have been made in the stability and homogeneity of the magnetic fields following the introduction of field stabilizers, shim coils, and sample spinning. Moreover, principal advances progressed the development of experiments (e.g. Carr–Purcell spin echoes, ^{13}C spectra at natural abundance) and theory (e.g. Bloch equations, effect of exchange on spectra, nuclear Overhauser effect (NOE), relaxation in the rotating frame, Solomon equations, Redfield theory of relaxation, spin temperature theory, Karplus theory for the dependence of three-bond J coupling on a dihedral angle, dependence of ^1H chemical shift on hydrogen bond strength). In 1958, Andrew observed that the broad ^{23}Na line in NaCl single crystals, arising from dipolar interactions, could be significantly narrowed by spinning the sample sufficiently fast. Moreover, he showed a dependence of the linewidth under spinning on $|0.5(3\cos^2\beta - 1)|$, with β the angle between the axis of rotation and the external magnetic field. Indeed, for $\beta = 54^\circ 44'$, the dipolar interaction effect on the linewidth was predicted to vanish as demonstrated experimentally in 1959 by Andrew himself (Andrew et al. 1959) and by Lowe (1959). As Andrew writes, “When we reported our first sample rotation results at the AMPERE Congress in Pisa in 1960, Professor Gorter of Leiden found the removal of the dipolar broadening of the NMR lines quite remarkable and referred to it as ‘magic,’ so we called the technique ‘magic angle spinning’ after that.” (Andrew 2007). The 1950s also saw a substantial passage of NMR from the hands of physicists to those of chemists, since the pioneering developments started to be successfully exploited in applications of NMR, mostly as a novel tool for chemical structure determination, especially thanks to the development of correlation charts between chemical shift and molecular functional groups and of the first theories trying to explain these correlations.

In the 1960s, spectrometers were further developed with the introduction of field-frequency lock (1961), superconducting magnets (1962), and time averaging (1963). Hartmann and Hahn (1962) suggested a method (and developed the corresponding theory) for transferring polarization between two different nuclear species (cross-polarization [CP]), which would reveal its extraordinary importance for the study of rare nuclei in solids only about 15 years later. Powles and Mansfield (1962) devised a simple two-pulse “solid echo” technique, able to refocus the quadrupolar and (to a good extent) the dipolar interaction in solids. Moreover, Goldburg and Lee (1963) showed how line narrowing in solids could be achieved not only by sample spinning as shown by Andrew a few years before but also by rotating radio-frequency (RF) fields, still at the magic angle. Stejskal and Tanner (1965) introduced pulsed field gradients (PFG), opening entirely new

perspectives for diffusion measurements. A few years later (1968), Waugh, Huber, and Haeberlen developed the WAHUHA pulse sequence, showing that it was able to remove homonuclear dipolar coupling by using a non-symmetrized combination of Hamiltonian states (Waugh et al. 1968), and at the same time, Waugh and Haeberlen also proposed the average Hamiltonian theory (AHT) (Haeberlen and Waugh 1968). All this considered, the biggest breakthrough of that decade was represented by the development of Fourier transform (FT) and pulsed methods: the first results, obtained by Ernst and Anderson at Varian Associates, were presented at the Experimental NMR Conference in Pittsburgh in 1965 and published in 1966 in the journal “Review of Scientific Instruments” (Ernst and Anderson 1966) after the same paper had been rejected twice by the Journal of Chemical Physics for being not sufficiently original. FT applied to NMR (FT NMR as we know it today), the main reason for the Nobel Prize in Chemistry awarded to Richard Ernst in 1991, quickly encountered widespread success due to the development, in the same years, of computers and software. In 1965, a new algorithm was developed at Bell Laboratories able to perform a FT of 4096 data points in approximately only 20 minutes!

During the 1970s, there was a huge increase in magnetic field strengths, and a ^1H Larmor frequency of 600 MHz was reached in 1977 in a non-superconducting magnet developed at Carnegie Mellon University. In 1973, the first paper concerning the use of NMR to obtain images by exploiting magnetic field gradients was published by Lauterbur (1973), who expanded the one-dimensional technique already proposed by Herman Carr in his PhD thesis more than 20 years before. In 2003, Lauterbur was awarded, together with Mansfield (who further contributed to the development of magnetic resonance imaging [MRI] soon after), the Nobel Prize in Medicine.¹ Another significant development made in the 1970s was the introduction of bidimensional techniques. Ernst developed an idea of Jeener, presented at an Ampère summer school in 1971 (and never transformed into a published paper), and published his first results in 1975. Due to the almost simultaneous development of MRI, the very first paper dealing with 2D techniques concerned their applications to imaging rather than spectroscopy (Kumar et al. 1975), but spectroscopic applications followed soon (Müller et al. 1975). On the solid’s front, first Mansfield, Rhim, Elleman, and Vaughan (Mansfield 1970; Rhim et al. 1973) and then Burum and Rhim (1979) improved the WAHUHA pulse sequence developing the MREV-8 and BR-24 pulse sequences for homonuclear dipolar decoupling. Moreover, separated local field (SLF) techniques, separately measuring correlated ^{13}C chemical shifts and dipolar interactions and representing a basis for the development of 2D techniques in solids, were first introduced by Waugh and coworkers in 1976 (Hester et al. 1976). All in all, the 1970s can claim the birth of “high-resolution SSNMR”: this can be considered coincident with the first experiments where the previously developed magic angle spinning (MAS), CP (based on the Hartmann–Hahn method), and

¹ This Nobel Prize was strongly protested by Raymond Vahan Damadian, who in 1971 had discovered that tumoral and normal tissues have different T_1/T_2 proton relaxation properties and had claimed that he proposed the idea of an MR body scanner. The echoes of the debate on whether Damadian would have deserved to share the 2003 Nobel Prize are still present in the scientific community.

heteronuclear dipolar decoupling techniques were combined together by Schaefer and Stejskal to obtain resolved spectra of rare nuclei, the first of which was the ^{13}C spectrum of poly(methyl methacrylate) (Schaefer and Stejskal 1976). Nevertheless, a fundamental contribution was made by Pines et al. a few years previously by successfully combining CP and decoupling techniques to obtain high-resolution static ^{13}C spectra of some organic solids, such as adamantane (Pines et al. 1972). Following Schaefer and Stejskal, MAS was also combined with homonuclear decoupling techniques to give the so-called combined rotation and multiple pulse spectroscopy (CRAMPS) experiment to obtain high-resolution spectra of abundant nuclei (Gerstein et al. 1977).

The 1980s were characterized by the rapid development of NMR in several fields and especially in the study of the tridimensional structure of biological macromolecules by solution-state NMR, for which the Nobel Prize in Chemistry was awarded to Kurt Wüthrich in 2002. Moreover, NMR started to be used as a diagnostic tool in medicine. The first apparatuses for fast field-cycling relaxation measurements in both liquids and solids were developed (Kimmich 1980; Noack 1986). Levitt and Freeman (1981) made significant improvements in the field of broadband decoupling, for instance, devising composite 180° inversion pulses and the MLEV cycle. Two-dimensional exchange techniques for studying structure and dynamics were introduced in the group of Spiess in 1986 (Schmidt et al. 1986). In the same year, the parahydrogen-enhanced methods for increasing NMR sensitivity were suggested for the first time (Bowers and Weitekamp 1986). At the end of that decade, both dynamic angle spinning (DAS) and double rotation (DOR) techniques were developed in Pines' group: they provided a solution for the line narrowing of the central transition of half-integer quadrupolar nuclei, which cannot be achieved by MAS alone (Samoson et al. 1988; Llor and Virlet 1988; Chmelka et al. 1989; Mueller et al. 1990). In the same years, Gullion and Schaefer (1989) devised the rotational echo double resonance (REDOR) technique for the direct measurement of heteronuclear dipolar coupling between isolated pairs of labeled nuclei. At the end of the 1980s, all the major companies were manufacturing spectrometers based on superconducting magnets up to 600 MHz.

The field strength had a further step upward in the first half of the next decade, with the first 800 MHz spectrometers commercialized in 1995. In the same year, the unilateral NMR scanner MOUSE (an acronym for mobile universal surface explorer) was built in Aachen (Eidmann et al. 1996). Still, in 1995, Frydman et al. (Frydman and Harwood 1995; Medek et al. 1995) introduced the multiple quantum magic angle spinning (MQMAS) technique, which suddenly revealed a huge improvement, with respect to DOR and DAS, in providing high-resolution NMR spectra of or achieving the line narrowing of the central transition of half-integer quadrupolar nuclei. Density functional theory (DFT) techniques started to be used for the computation of chemical shifts, and in this regard, a great improvement for the study of solids was provided by the development of gauge-including projector-augmented wave (GIPAW) methods in 2001 (Pickard and Mauri 2001).

In the twenty-first century, the use of SSNMR became much more widespread: the number of SSNMR-related publications increased by more than three times

from the last decade of the twentieth century to the first of the twenty-first century, passing from about 1000 publications/year on average to about 3500, further raised to about 4400 per year in the second decade of the twenty-first century. Along with further increases in magnetic field strengths (nowadays reaching a proton Larmor frequency of 1.2 GHz), several new techniques were developed or “rediscovered” for the study of solids. The group of Samoson obtained significant improvements in MAS frequencies and advanced the CryoMAS probe for standard CP-based experiments in structural biology (Samoson et al. 2005). At the moment of writing, a MAS frequency of 110–111 kHz has been reached on commercial MAS probes using rotors with a diameter of 0.70–0.75 mm, while CryoMAS probes with different designs have also been developed in Southampton and Bethesda laboratories and are also commercialized. Hyperpolarization methods, in particular parahydrogen-induced polarization (PHIP) and dynamic nuclear polarization (DNP), although very well-known since the 1980s and the 1950s, respectively, recently demonstrated an extraordinary revival. This resulted in the development of commercial DNP-NMR spectrometers: the potentially wide application of DNP for obtaining NMR spectra with a signal-to-noise ratio increased by some orders of magnitude, even in solids, is nowadays clearly recognized and feasible (Rankin et al. 2019). Moreover, microcoils, already applied in MRI and solution-state NMR, have also recently found usefulness in solids, and a brilliant new technique has been developed by Sakellariou, based on spinning the microcoil, put within the MAS rotor, and on inductive coupling (Sakellariou et al. 2007).

1.2 Basic Description of NMR Spectroscopy

NMR and electron paramagnetic resonance (EPR) spectroscopies probe the states of inherent magnetic properties of the materials under investigation. Such magnetic resonance methods differ from optical spectroscopy, as the samples interact with the magnetic component of the electromagnetic radiation, while in the latter case, the electric field component is involved. Moreover, resonance spectroscopies examine transitions between spin states in a static magnetic field, required to lift their degeneracy. In particular, since the energy differences between nuclear spin states are very small, NMR spectroscopy is located at the low-frequency end (i.e. the RF range) of the electromagnetic spectrum (Figure 1.1). For this reason, saturation effects, relaxation, and related phenomena play important roles in NMR spectroscopy, while they are of minor importance for spectroscopies at higher frequencies.

In addition to the static magnetic field, an oscillatory magnetic field, arising from the RF pulsed irradiation, induces transitions between the spin states from which the NMR signal is derived. The basic NMR spectrometer consists of (i) a strong external magnetic field, (ii) an RF source, (iii) a probe that goes inside the external magnetic field and includes a coil which surrounds the sample, with the axis defining the direction of the oscillatory magnetic field perpendicular to the external field direction, used for both RF irradiation of the sample and detection of the signal, (iv) a receiver unit, and (v) a computer. As will be outlined later, the detected

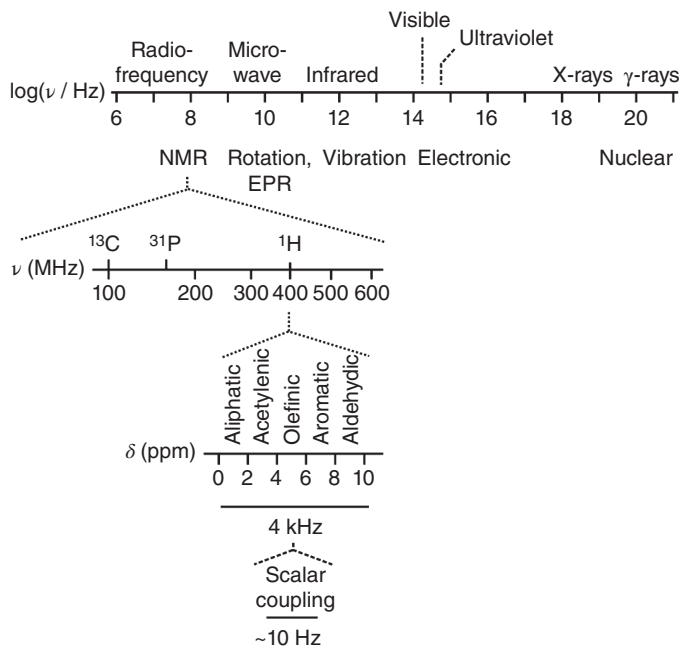


Figure 1.1 The electromagnetic spectrum and expansion of the NMR radio-frequency range to show typical frequencies for different isotopes and for ^1H nuclei in different chemical environments.

time-dependent signal is converted to the NMR spectrum, which contains the relevant information about the sample under investigation.

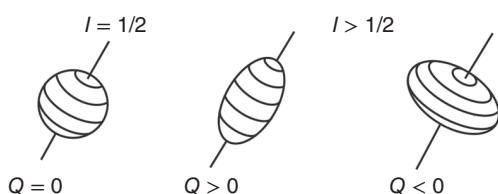
One basic requirement for NMR spectroscopy is a sample with a certain amount of nuclei (typically 10^{18} – 10^{20}) with non-zero nuclear spin I . The periodic chart in Figure 1.2 demonstrates that for the majority of chemical elements one or more isotopes are found, in their most stable nuclear spin configuration², with non-null nuclear spin. The respective spin quantum number can assume integer or half-integer values depending on the number of protons and neutrons forming the nucleus (Table 1.1). Quadrupolar nuclei possess a spin quantum number I greater than $1/2$ and are characterized by a nonspherical, oblate or prolate, nuclear charge distribution with positive or negative nuclear quadrupole moment Q , respectively (Figure 1.3). Interaction with the electric field from nearby electrons gives rise to the so-called quadrupolar interaction, which plays a prominent role in SSNMR spectroscopy and for spin relaxation.

² Each isotope can give rise to different nuclear spin configurations, which correspond to different combinations of the spins of neutrons and protons and, consequently, to different spin quantum numbers. The different configurations are characterized by huge energy separations (tens of keV, 10–11 orders of magnitude larger than those involved in NMR), and the transitions among them are studied by the Mössbauer spectroscopy, making use of γ -rays. Considering that only the fundamental configuration is populated in normal conditions, in this book, we will use the short expression “spin quantum number of an isotope” referring to the spin quantum number of its fundamental configuration.



Table 1.1 Nuclear spin of the fundamental configuration depending on the number of protons and neutrons of the isotope.

Number of protons (atomic number, Z)	Number of neutrons (N)	Atomic mass ($Z + N$)	Nuclear spin (I)
Odd	Even	Odd	Half-integer
Even	Odd	Odd	Half-integer
Even	Even	Even	0
Odd	Odd	Even	Integer > 0

**Figure 1.3** Charge distribution for non-quadrupolar ($I = 1/2$) and quadrupolar ($I > 1/2$) nuclei. Q is the nuclear quadrupole moment.

1.2.1 Nuclear Spins and Nuclear Zeeman Effect

The nuclear magnetic moment $\vec{\mu}$ represents a central quantity in NMR spectroscopy that is parallel or antiparallel to the nuclear spin \vec{I}

$$\vec{\mu} = \hbar\gamma_N\vec{I} \quad (1.1)$$

depending on the sign of the nuclear gyromagnetic ratio γ_N with

$$\gamma_N = \frac{g_N\mu_N}{\hbar} = \frac{eg_N}{2m_N} \quad (1.2)$$

and

$$m_N = 1.67 \times 10^{-27} \text{ kg}; e = +1.6 \times 10^{-19} \text{ C} \quad (1.3)$$

Here, $\mu_N = e\hbar/2m_N$, g_N , e , and m_N are the nuclear magneton, the nuclear g -factor, the elementary charge, and the proton mass, respectively. $\hbar = h/2\pi = 1.05 \times 10^{-34} \text{ J}\cdot\text{s}$ is the reduced Planck's constant.

In the presence of a strong external magnetic field (characterized by the magnetic flux density \vec{B}), each orientation of the magnetic moment is accompanied by a different potential energy. The resulting Zeeman contribution to the total energy is thus given by the scalar product

$$E = -\vec{\mu}\cdot\vec{B} = -|\vec{\mu}||\vec{B}|\cos\theta \quad (1.4)$$

where θ is the angle between $\vec{\mu}$ and \vec{B} . For a homogeneous magnetic field pointing along the z_L direction (L , laboratory frame), the flux density has only one component with

$$\vec{B} = \begin{pmatrix} 0 \\ 0 \\ B_0 \end{pmatrix} \quad (1.5)$$

from which a nuclear Zeeman energy of

$$E = -\hbar\gamma_N \left| \vec{B} \right| \left| \vec{I} \right| \cos\theta = -\hbar\gamma_N B_0 I_z \quad (1.6)$$

results. Here, I_z is the component of the nuclear spin vector \vec{I} along the z_L direction.

So far, Eq. (1.6), arising from classical physics, does not consider any restriction for the values of $\left| \vec{I} \right|$ and I_z . However, quantum mechanics provides a quantization of both these quantities according to

$$\left| \vec{I} \right| = \sqrt{I(I+1)} \quad (1.7)$$

$$I_z = m_I \quad (1.8)$$

The nuclear spin quantum number I can assume integer or semi-integer values, while m_I ranges from $-I$ to $+I$ with intervals of 1, and therefore, it can assume $2I+1$ different values. In the absence of an external magnetic field, these $2I+1$ different values correspond to degenerate energy levels. In contrast, in a homogeneous external magnetic field, the degeneracy in different spin energy levels is lifted, and after insertion of Eq. (1.8) into Eq. (1.6), the energy results to be

$$E_{m_I} = -\hbar\gamma_N B_0 m_I \quad (1.9)$$

In the case of an $I = 1/2$ spin system, the two allowed magnetic spin quantum numbers $m_I = 1/2$ and $-1/2$ correspond to two energy-separated states (Figure 1.4a), typically indicated as α and β states, respectively.

The above-mentioned expression for the Zeeman energy is formally obtained by inserting the appropriate Hamiltonian into the Schrödinger equation $\hat{H}\psi = E\psi$, which is then solved on the basis of appropriate eigenfunctions, the spin functions $|I, m_I\rangle$ (see Chapter 2). For instance, for $I = 1/2$ nuclei, the two eigenfunctions are $|\alpha\rangle = |1/2, 1/2\rangle$ and $|\beta\rangle = |1/2, -1/2\rangle$. Inserting the Zeeman Hamiltonian

$$\hat{H} = -\hbar\gamma_N B_0 \hat{I}_z \quad (1.10)$$

into the Schrödinger equation yields

$$-\hbar\gamma_N B_0 \hat{I}_z |I, m_I\rangle = E_{m_I} |I, m_I\rangle \quad (1.11)$$

which provides the energy eigenvalues E_{m_I} of Eq. (1.9).

As will be more extensively discussed in Section 1.2.4 and in Chapter 2, the states described by the eigenfunctions of the Zeeman Hamiltonian (Zeeman states) are not the only possible states for the nuclear spins, all their linear combinations (superposition states) being allowed as well. This subject will be further dealt with later. However, for most of the subjects treated in this chapter, the assumption of the existence of Zeeman states only (found in several textbooks, although not rigorously correct) does not change the terms of the discussion.

In general, NMR spectroscopy deals with transitions between various magnetic energy levels caused by (i) excitation with (external) electromagnetic irradiation in the RF range and (ii) relaxation effects. The time-dependent perturbation theory provides the selection rule for spin transitions during RF irradiation

$$\Delta m_I = \pm 1 \quad (1.12)$$

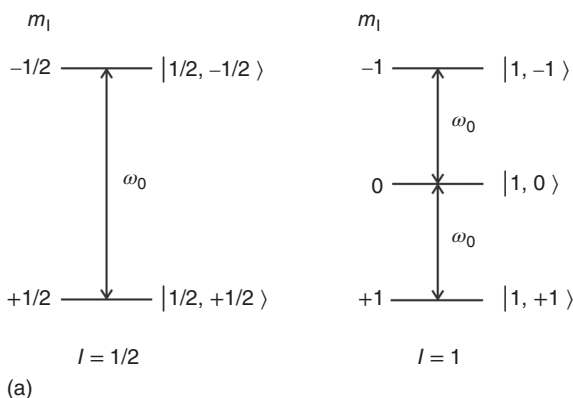
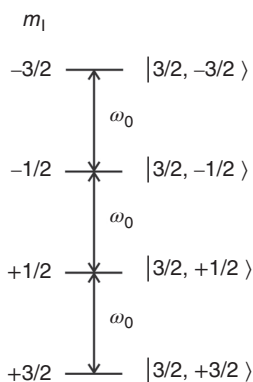


Figure 1.4 Energy separation of the spin states caused by the external magnetic field B_0 and possible transitions between them for the cases: (a) $I = 1/2$ and $I = 1$; (b) $I = 3/2$. In all cases, $\gamma_N > 0$ has been assumed.



(b) $I = 3/2$

Insertion of this result into Eq. (1.9) yields the *resonance condition*

$$|\Delta E| = \hbar |\gamma_N| |\Delta m_I| B_0 = \hbar \omega_0 = h\nu_0 \quad (1.13)$$

or, in angular frequency units,

$$\omega_0 = |\gamma_N| B_0 \quad (1.14)$$

The selection rule indicates that only transitions between adjacent nuclear spin states are allowed (Figure 1.4). In the case of a half-integer quadrupolar nucleus, it is further distinguished between central ($1/2 \leftrightarrow -1/2$, CT) and satellite transitions (all but the central one, e.g. $3/2 \leftrightarrow 1/2$, $-1/2 \leftrightarrow -3/2$ in Figure 1.4b, ST). In Eq. (1.14), ω_0 is the so-called *Larmor frequency*, which characterizes the frequency separation between adjacent nuclear spin states. The Larmor frequency ω_0 plays an important role in NMR experiments, as will be briefly considered next.

Nuclear spins – as is also true for the electron spin – possess an angular momentum \vec{L}

$$\vec{L} = \vec{I}\hbar = \frac{\vec{\mu}}{\gamma_N} \quad (1.15)$$

Following classical physics, in an external magnetic field \vec{B} , an angular momentum \vec{L} experiences a torque \vec{D} , describing the change of \vec{L} with time, perpendicular to the plane defined by z_L and the direction of \vec{L}

$$\vec{D} = \frac{d\vec{L}}{dt} = \frac{d(\vec{I}\hbar)}{dt} = \vec{\mu} \times \vec{B} \quad (1.16)$$

with modulus

$$|\vec{D}| = |\vec{\mu}| |\vec{B}| \sin \theta \quad (1.17)$$

The torque causes precession of the nuclear spins and magnetic moments around the magnetic field direction (z_L) (Figure 1.5), at angular frequency

$$\vec{\omega}_0 = -\gamma_N \vec{B} \quad (1.18)$$

with the same absolute value found for the separation of adjacent Zeeman states in Eq. (1.14)

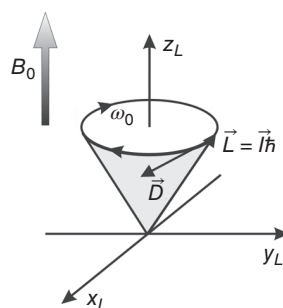
$$\omega_0 = \frac{|\vec{D}|}{|\vec{L}| \sin \theta} = |\gamma_N| B_0 \quad (1.19)$$

The Larmor frequency thus represents a characteristic property of each nuclear spin and only depends on the gyromagnetic ratio and the strength of the external magnetic field. The direction of precession is determined by the sign of the gyromagnetic ratio. Following the “right-hand rule,”³ the precession is clockwise, as shown in Figure 1.5, for nuclear spins with $\gamma_N > 0$ and counterclockwise for spins with $\gamma_N < 0$. Typical values for the Larmor frequency $\nu_0 = \omega_0/2\pi$ are in the RF range between about 20 MHz and 1 GHz (see Table 1.2, where the Larmor frequencies for a magnetic field strength of $B_0 = 11.7433$ T, along with the main nuclear properties, are reported for a variety of isotopes with non-null spin).

1.2.2 Spin Ensembles

In a real NMR experiment, about 10^{18} – 10^{20} or even more spins are present in the sample, and the characteristic properties of spin ensembles have to be discussed instead of those of an isolated spin. Hence, the nuclear spins have to be distributed

Figure 1.5 Representation of torque (\vec{D}) and angular velocity ($\vec{\omega}_0$) vectors arising from the interaction of the magnetic moment associated with the nuclear spin and the external magnetic field.



3 This rule states that if we align the thumb of the right hand with the rotation axis, then the positive sense of rotation is that indicated by the wrapping around of the other fingers of the hand.

Table 1.2 Main nuclear properties of principal isotopes with non-null spin.

Element	Atomic no.	Mass no.	Spin	Natural abundance (%)	γ_N (rad s ⁻¹ T ⁻¹ · 10 ⁻⁷)	ν_0 @11.7433 T (MHz)	Quadrupolar moment, Q (fm ²)
H	1	1	1/2	99.9885	26.752 2128	500.000	
H	1	2	1	0.0115	4.106 627 91	76.753	0.285783 ^a
He	2	3	1/2	0.000 137	-20.380 1587	380.906	
Li	3	6	1	7.59	3.937 1709	73.586	-0.0808
Li	3	7	3/2	92.41	10.397 7013	194.333	-4.01
Be	4	9	3/2	100	-3.759 666	70.268	5.288
B	5	10	3	19.9	2.874 6786	53.728	8.459
B	5	11	3/2	80.1	8.584 7044	160.448	4.059
C	6	13	1/2	1.07	6.728 284	125.752	
N	7	14	1	99.632	1.933 7792	36.142	2.044
N	7	15	1/2	0.368	-2.712 618 04	50.699	
O	8	17	5/2	0.038	-3.628 08	67.809	-2.558
F	9	19	1/2	100	25.181 48	470.643	
Ne	10	21	3/2	0.27	-2.113 08	39.494	10.155
Na	11	23	3/2	100	7.080 8493	132.341	10.4
Mg	12	25	5/2	10.00	-1.638 87	30.631	19.94
Al	13	27	5/2	100	6.976 2715	130.387	14.82 ^b
Si	14	29	1/2	4.6832	-5.3190	99.412	
P	15	31	1/2	100	10.8394	202.589	
S	16	33	3/2	0.76	2.055 685	38.421	-6.94 ^a
Cl	17	35	3/2	75.78	2.624 198	49.046	-8.112 ^a
Cl	17	37	3/2	24.22	2.184 368	40.826	-6.393 ^a
K	19	39	3/2	93.2581	1.250 0608	23.364	6.03 ^a
K	19	41	3/2	6.7302	0.686 068 08	12.823	7.34 ^a
Ca	20	43	7/2	0.135	-1.803 069	33.699	-4.08
Sc	21	45	7/2	100	6.508 7973	121.650	-22.0
Ti	22	47	5/2	7.44	-1.5105	28.231	30.2
Ti	22	49	7/2	5.41	-1.510 95	28.240	24.7
V	23	51	7/2	99.750	7.045 5117	131.681	-5.2
Cr	24	53	3/2	9.501	-1.5152	28.319	-15.0
Mn	25	55	5/2	100	6.645 2546	124.200	33.0
Fe	26	57	1/2	2.119	0.868 0624	16.224	
Co	27	59	7/2	100	6.332	118.345	42.0
Ni	28	61	3/2	1.1399	-2.3948	44.759	16.2
Cu	29	63	3/2	69.17	7.111 7890	132.920	-22.0

(Continued)

Table 1.2 (Continued)

Element	Atomic no.	Mass no.	Spin	Natural abundance (%)	γ_N (rad s ⁻¹ T ⁻¹ · 10 ⁻⁷)	ν_0 @11.7433 T (MHz)	Quadrupolar moment, Q (fm ²)
Cu	29	65	3/2	30.83	7.604 35	142.126	-20.40
Zn	30	67	5/2	4.10	1.676 688	31.337	12.2 ^a
Ga	31	69	3/2	60.108	6.438 855	120.342	17.1
Ga	31	71	3/2	39.892	8.181 171	152.906	10.7
Ge	32	73	9/2	7.73	-0.936 0303	17.494	-19.6
As	33	75	3/2	100	4.596 163	85.902	31.1 ^a
Se	34	77	1/2	7.63	5.125-3857	95.794	
Br	35	79	3/2	50.69	6.725 616	125.702	30.87 ^a
Br	35	81	3/2	49.31	7.249 776	135.499	25.79 ^a
Kr	36	83	9/2	11.49	-1.033 10	19.309	25.9
Rb	37	85	5/2	72.17	2.592 7050	48.458	27.6
Rb	37	87	3/2	27.83	8.786 400	164.218	13.35
Sr	38	87	9/2	7.00	-1.163 9376	21.754	30.5 ^a
Y	39	89	1/2	100	-1.316 2791	24.601	
Zr	40	91	5/2	11.22	-2.497 43	46.677	-17.6
Nb	41	93	9/2	100	6.5674	122.745	-32.0
Mo	42	95	5/2	15.92	-1.751	32.726	-2.2
Mo	42	97	5/2	9.55	-1.788	33.418	25.5
Ru	44	99	5/2	12.76	-1.229	22.970	7.9
Ru	44	101	5/2	17.06	-1.377	25.736	45.7
Rh	45	103	1/2	100	-0.8468	15.827	
Pd	46	105	5/2	22.33	-1.23	22.989	66.0
Ag	47	107	1/2	51.839	-1.088 9181	20.352	
Ag	47	109	1/2	48.161	-1.251 8634	23.397	
Cd	48	111	1/2	12.80	-5.698 3131	106.502	
Cd	48	113	1/2	12.22	-5.960 9155	111.410	
In	49	113	9/2	4.29	5.8845	109.982	76.1 ^a
In	49	115	9/2	95.71	5.8972	110.219	77.2 ^a
Sn	50	117	1/2	7.68	-9.588 79	179.215	
Sn	50	119	1/2	8.59	-10.0317	187.493	
Sb	51	121	5/2	57.21	6.4435	120.429	-54.3 ^a
Sb	51	123	7/2	42.79	3.4892	65.213	-69.2 ^a
Te	52	123	1/2	0.89	-7.059 098	131.935	
Te	52	125	1/2	7.07	-8.510 8404	159.068	
I	53	127	5/2	100	5.389 573	100.731	-68.822 ^a

(Continued)

Table 1.2 (Continued)

Element	Atomic no.	Mass no.	Spin	Natural abundance (%)	γ_N (rad s ⁻¹ T ⁻¹ · 10 ⁻⁷)	ν_0 @11.7433 T (MHz)	Quadrupolar moment, Q (fm ²)
Xe	54	129	1/2	26.44	-7.452 103	139.280	
Xe	54	131	3/2	21.18	2.209 076	41.288	-11.46 ^a
Cs	55	133	7/2	100	3.533 2539	66.037	-0.343
Ba	56	135	3/2	6.592	2.675 50	50.005	15.3 ^a
Ba	56	137	3/2	11.232	2.992 95	55.938	23.6 ^a
La	57	139	7/2	99.910	3.808 3318	71.178	20.6 ^a
Pr	59	141	5/2	100	8.1907	153.085	-5.89
Nd	60	143	7/2	12.2	-1.457	27.231	-63.0
Nd	60	145	7/2	8.3	-0.898	16.784	-33.0
Sm	62	147	7/2	14.99	-1.115	20.839	-25.9
Sm	62	149	7/2	13.82	-0.9192	17.180	7.5 ^a
Eu	63	151	5/2	47.81	6.6510	124.307	90.3
Eu	63	153	5/2	52.19	2.9369	54.891	241.2
Gd	64	155	3/2	14.80	-0.821 32	15.351	127.0
Gd	64	157	3/2	15.65	-1.0769	20.127	135.0
Tb	65	159	3/2	100	6.431	120.196	143.2
Dy	66	161	5/2	18.91	-0.9201	17.197	250.7
Dy	66	163	5/2	24.90	1.289	24.091	264.8
Ho	67	165	7/2	100	5.710	106.720	358.0
Er	68	167	7/2	22.93	-0.771 57	14.421	356.5
Tm	69	169	1/2	100	-2.218	41.455	
Yb	70	171	1/2	14.28	4.7288	88.381	
Yb	70	173	5/2	16.13	-1.3025	24.344	280.0
Lu	71	175	7/2	97.41	3.0552	57.102	349.0
Lu	71	176	7	2.59	2.1684	40.527	497.0
Hf	72	177	7/2	18.60	1.086	20.297	336.5
Hf	72	179	9/2	13.62	-0.6821	12.748	379.3
Ta	73	181	7/2	99.988	3.2438	60.627	317.0
W	74	183	1/2	14.31	1.1282 403	21.087	
Re	75	185	5/2	37.40	6.1057	114.116	218.0
Re	75	187	5/2	62.60	6.1682	115.284	207.0
Os	76	187	1/2	1.96	0.619 2895	11.575	
Os	76	189	3/2	16.15	2.107 13	39.382	85.6
Ir	77	191	3/2	37.3	0.4812	8.994	81.6

(Continued)

Table 1.2 (Continued)

Element	Atomic no.	Mass no.	Spin	Natural abundance (%)	γ_N (rad s ⁻¹ T ⁻¹ · 10 ⁻⁷)	ν_0 @11.7433 T (MHz)	Quadrupolar moment, Q (fm ²)
Ir	77	193	3/2	62.7	0.5227	9.769	75.1
Pt	78	195	1/2	33.832	5.8385	109.122	
Au	79	197	3/2	100	0.473 060	8.842	54.7
Hg	80	199	1/2	16.87	4.845 7916	90.568	
Hg	80	201	3/2	13.18	-1.788 769	33.432	38.7 ^a
Tl	81	203	1/2	29.524	15.539 3338	290.431	
Tl	81	205	1/2	70.476	15.692 1808	293.288	
Pb	82	207	1/2	22.1	5.580 46	104.299	
Bi	83	209	9/2	100	4.3750	81.769	-51.6
U	92	235	7/2	0.7200	-0.52	9.719	493.6

Source: Harris et al. (2001, 2008), with the exception of some updated values of quadrupolar moments, which were taken from ^aPyykkö (2018) and ^bAerts and Brown (2019).

among the allowed spin states, defined by the aforementioned magnetic spin quantum numbers. For a system at thermal equilibrium, this can be done by following the Boltzmann distribution (Figure 1.6). For an $I = 1/2$ spin system, the populations for the α or β spin states are given by

$$\frac{n_i}{N} = \frac{\exp(-E_i/kT)}{\exp(-E_\alpha/kT) + \exp(-E_\beta/kT)} \quad (1.20)$$

where $N = n_\alpha + n_\beta$ is the total number of spins, $i = \alpha$ or β , k is the Boltzmann constant (1.38×10^{-23} J K⁻¹), and T is the absolute temperature. In the above equation, the exponentials can be developed in a power series. Since the absolute values of the spin energies E_i (Eq. (1.9)) are much smaller than kT , it is possible to neglect

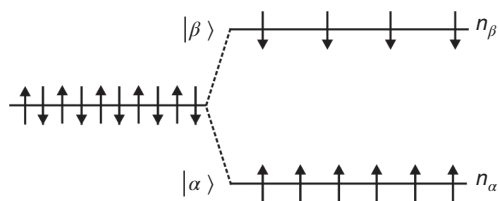


Figure 1.6 Schematic representation of the populations of the two states of a spin-1/2 nucleus in the absence (left, degenerate levels) and presence (right, different energy levels) of an external magnetic field. The “up” and “down” arrows indicate the states α ($m_I = +1/2$) and β ($m_I = -1/2$), respectively. It should be noted that equal populations are present in the absence of the magnetic field, while the population of α is greater than that of β in its presence (the difference of populations is here greatly exaggerated: as explained in the text, typical differences are of about a few tens over 1 million nuclei).

the third and all higher terms of the power series (high-temperature approximation) yielding

$$\begin{aligned} n_\alpha &= \frac{1}{2}N \left(1 + \frac{\hbar\gamma_N B_0}{2kT} \right) \\ n_\beta &= \frac{1}{2}N \left(1 - \frac{\hbar\gamma_N B_0}{2kT} \right) \end{aligned} \quad (1.21)$$

With a typical value $B_0 = 9.4$ T and ^1H nuclei at room temperature, a ratio of

$$\frac{n}{N} = 3.2 \times 10^{-5} \quad (1.22)$$

is obtained, where $n = n_\alpha - n_\beta$. That is, out of 10^6 spins, the energetically more favorable α spin state possesses only 32 spins more than the β spin state. This very small population difference between nuclear spin states is a result of the relatively weak Zeeman interaction and the main reason for the inherently low sensitivity of NMR spectroscopy.

As a further consequence of the spin ensemble, the individual magnetic moments have to be replaced by the sum over all magnetic moments, which yields the magnetization \vec{M}

$$\vec{M} = \sum_i \vec{\mu}_i \quad (1.23)$$

As will be discussed below, at thermal equilibrium in a strong external magnetic field, there is a net longitudinal magnetization along the z_L -axis, while there is no net magnetization on the x_L - y_L plane; therefore, the equilibrium magnetization M_0 points along the z_L direction, parallel to the external magnetic field. For the $I = 1/2$ case, one finds

$$M_0 = M_{z,L} = N \frac{\gamma_N^2 \hbar^2}{4kT} B_0 \quad (1.24)$$

and for a general spin system, the Curie law holds true:

$$M_0 = N \frac{I(I+1) \gamma_N^2 \hbar^2}{3kT} B_0 = \frac{C_N B_0}{T} \quad (1.25)$$

where

$$C_N = N \frac{I(I+1) \gamma_N^2 \hbar^2}{3k} \quad (1.26)$$

is the Curie constant.

The magnetization can be used to calculate the contribution from the nuclear spins to the sample magnetism, as expressed by the susceptibility

$$\chi_{\text{nucl}} = \frac{M_0}{B_0} = N \frac{I(I+1) \gamma_N^2 \hbar^2}{3kT} \quad (1.27)$$

It turns out that this nuclear paramagnetism ($\chi_{\text{nucl}} > 0$) is very small with values for χ_{nucl} in the order of about 10^{-9} . In fact, the major contribution to sample magnetism arises from the electrons (electronic currents and magnetic moments). Most materials are diamagnetic ($\chi < 0$), with susceptibility absolute values of about 10^{-6} to 10^{-5} , which greatly exceed the contribution from the nuclear paramagnetism.

It is the magnetization that determines the final NMR signal intensity. The NMR signal intensity is thus inversely proportional to the temperature (as a result of the

Boltzmann distribution) and proportional to the strength of the external magnetic field, to the square of the gyromagnetic ratio, and to the number of NMR-active nuclei under observation (to which the isotopic natural abundance gives a very important contribution).

The transverse magnetization components along the x_L and the y_L directions are zero due to the absence of any phase relationship among the individual spins. That is, although each spin (in the various spin states) undergoes a precession around the z_L -axis, the individual spins point in a different direction at each moment. The vanishing transverse components are thus not a result of an averaging effect in time due to the individual precession of the separate spins. Rather, they reflect an absence of phase relationship among the individual spins.

Although in thermal equilibrium with only an external magnetic field, transverse magnetization is zero, this quantity is nevertheless very important, as it is the transverse magnetization that is detected during the NMR experiment and that provides all relevant information about the spin system under investigation. As will be shown below, transverse magnetization is created as soon as the sample is irradiated by a transverse electromagnetic field of appropriate frequency.

1.2.3 Single Pulse Experiment, Bloch Equations, and Fourier Transformation

NMR spectroscopy is normally carried out in FT (or pulsed) mode and starts from the equilibrium magnetization mentioned above. Here, irradiation of the sample by an external time-dependent magnetic field – in the most general case RF pulses of different duration, frequency, amplitude, and phase – disturbs and actively manipulates the equilibrium magnetization in a directed way. At the end of the experiment, the time-dependent transverse magnetization is detected as an electric signal, the free induction decay (FID), which is then Fourier transformed to give the NMR spectrum. Frequently, the FID is recorded as a function of another time variable (e.g. relaxation experiments) or of constant time increments (e.g. 2D and multidimensional experiments).

The basic NMR experiment, the single pulse experiment, will be briefly described next by employing the Bloch equations. Here, the transverse magnetization is detected immediately after an RF pulse (Figure 1.7). As outlined earlier, the spin possesses an angular momentum \vec{L} and a torque \vec{D} is exerted on the spin/magnetic moment in the presence of a magnetic field (see Eq. (1.16)), which yields the equation of motion for a single magnetic moment

$$\frac{d\vec{\mu}}{dt} = \gamma_N (\vec{\mu} \times \vec{B}) \quad (1.28)$$

and for the macroscopic magnetization

$$\frac{d\vec{M}}{dt} = \gamma_N (\vec{M} \times \vec{B}) \quad (1.29)$$

The contributions to the total magnetic field arise from the external static magnetic field along the z_L direction and from an oscillating magnetic field in the sample coil due to sample irradiation in the RF range. The latter magnetic field component is

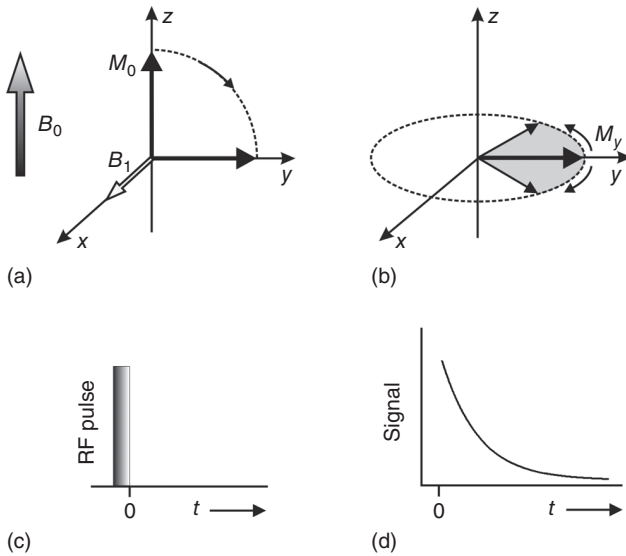


Figure 1.7 The basic NMR experiment: (a) the equilibrium magnetization is flipped on the z - y plane by 90° following the application of an RF pulse (c) applied along x with suitable intensity B_1 and duration. (b, d) After turning off the RF pulse, the net magnetization along y , detected as FID, decreases as a result of the dephasing of its components.

linearly polarized in the x_L -direction and is modulated in time by ω_{rf}

$$\vec{B}_1^{\text{rf}}(t) = \begin{pmatrix} 2B_1 \cos \omega_{\text{rf}}t \\ 0 \\ 0 \end{pmatrix} \quad (1.30)$$

The linear component can be seen as the superposition of two circular polarized components $\vec{B}_1^{\text{left}}(t)$ and $\vec{B}_1^{\text{right}}(t)$, rotating in opposite directions in the x_L - y_L plane.

$$\vec{B}_1^{\text{rf}}(t) = \vec{B}_1^{\text{right}}(t) + \vec{B}_1^{\text{left}}(t) \quad (1.31)$$

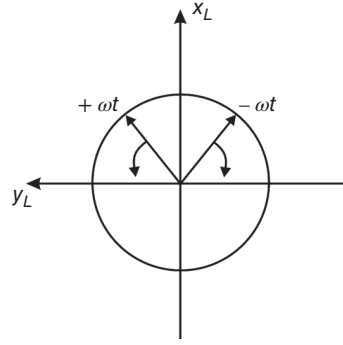
with

$$\vec{B}_1^{\text{left}}(t) = \begin{pmatrix} B_1 \cos \omega_{\text{rf}}t \\ B_1 \sin \omega_{\text{rf}}t \\ 0 \end{pmatrix}$$

$$\vec{B}_1^{\text{right}}(t) = \begin{pmatrix} B_1 \cos \omega_{\text{rf}}t \\ -B_1 \sin \omega_{\text{rf}}t \\ 0 \end{pmatrix} \quad (1.32)$$

as shown in Figure 1.8. During the NMR experiment, only the B_1 component that possesses the same sense of rotation as the considered nuclear spins is relevant. For nuclear spins with a positive gyromagnetic ratio ($\gamma_N > 0$), this would be the $\vec{B}_1^{\text{right}}(t)$ component, while for the nuclei with $\gamma_N < 0$, it would be the $\vec{B}_1^{\text{left}}(t)$ component. The other, nonresonant component, rotating in the opposite sense, can be neglected to a good approximation (see Section 3.2).

Figure 1.8 The two counter-rotating components of \vec{B}_1 represented in the laboratory frame.



For the derivation made in this chapter, from now on, we will assume $\gamma_N > 0$, therefore using the expression of the $\vec{B}_1^{\text{right}}(t)$ component. Accordingly, the total magnetic field will be given by

$$\vec{B}(t) = \begin{pmatrix} B_1 \cos \omega_{\text{rf}} t \\ -B_1 \sin \omega_{\text{rf}} t \\ B_0 \end{pmatrix} \quad (1.33)$$

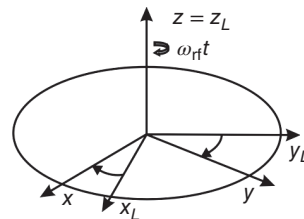
After inserting this expression into Eq. (1.29) and introducing two phenomenological relaxation terms with time constants T_1 and T_2 , which take into account the return of longitudinal and transverse magnetization components to their equilibrium values, the general Bloch equations are obtained that describe the time evolution of the magnetization in the presence of a static external magnetic field and a time-dependent RF field

$$\begin{aligned} \frac{dM_{x,L}}{dt} &= \gamma_N (M_{y,L} B_0 + M_{z,L} B_1 \sin \omega_{\text{rf}} t) - \frac{M_{x,L}}{T_2} \\ \frac{dM_{y,L}}{dt} &= -\gamma_N (M_{x,L} B_0 - M_{z,L} B_1 \cos \omega_{\text{rf}} t) - \frac{M_{y,L}}{T_2} \\ \frac{dM_{z,L}}{dt} &= -\gamma_N (M_{x,L} B_1 \sin \omega_{\text{rf}} t + M_{y,L} B_1 \cos \omega_{\text{rf}} t) - \frac{M_{z,L} - M_0}{T_1} \end{aligned} \quad (1.34)$$

Solution of the Bloch equations is achieved by the transformation from the laboratory frame $\{x_L, y_L, z_L\}$ (defined by the external magnetic field) to the rotating frame $\{x, y, z\}$ that rotates at frequency ω_{rf} around the external field direction (Figure 1.9). The connection between the transverse magnetization components in the laboratory frame ($M_{x,L}, M_{y,L}$) and rotating frame (M_x, M_y) is given by

$$\begin{aligned} M_x &= M_{x,L} \cos \omega_{\text{rf}} t - M_{y,L} \sin \omega_{\text{rf}} t \\ M_y &= M_{x,L} \sin \omega_{\text{rf}} t + M_{y,L} \cos \omega_{\text{rf}} t \end{aligned} \quad (1.35)$$

Figure 1.9 Representation of the $\{x_L, y_L, z_L\}$ laboratory and $\{x, y, z\}$ rotating frames.



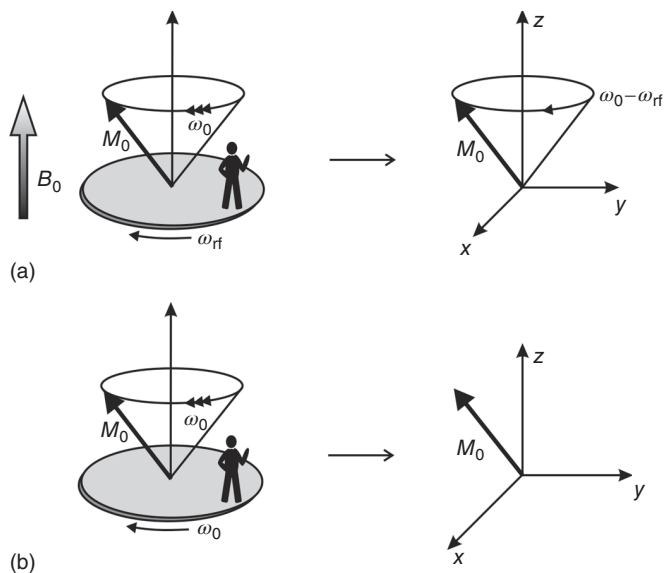


Figure 1.10 Evolution of the magnetization in the laboratory (left) and rotating (right) frames. (a) The rotating frame rotates at a frequency $\omega_{\text{rf}} < \omega_0$ about the z -axis, and therefore, the magnetization precesses in the rotating frame with a frequency $\omega_0 - \omega_{\text{rf}}$. (b) The rotating frame rotates at a frequency $\omega_{\text{rf}} = \omega_0$ about the z -axis, and therefore, the magnetization is static in the rotating frame.

The rotating frame plays an important role in NMR spectroscopy as it is the reference frame for the discussion of all NMR experiments. In the rotating frame, the magnetization precesses around the external magnetic field at a frequency $\omega_0 - \omega_{\text{rf}}$ and therefore the “effective” external magnetic field along z is

$$\Delta B = B_0 - B_{\text{rot}} = B_0 - \frac{\omega_{\text{rf}}}{\gamma_N} \quad (1.36)$$

This situation is illustrated in Figure 1.10. If the frequency of the rotating frame ω_{rf} is identical to the Larmor frequency ω_0 , the magnetization no longer precesses about z (Figure 1.10b). Also, considering the presence of B_1 , its time dependence is removed in the rotating frame, and when the effective external magnetic field along z is null, only a “static” B_1 component along x remains. However, for the most general case, an effective magnetic field B_{eff} is present, which lies in the x - z plane, the absolute direction of which depends on the relative size of B_1 and ΔB , as indicated in Figure 1.11.

$$\vec{B}_{\text{eff}} = \begin{pmatrix} B_1 \\ 0 \\ B_0 - \omega_{\text{rf}}/\gamma_N \end{pmatrix} = \begin{pmatrix} B_1 \\ 0 \\ B_0(1 - \omega_{\text{rf}}/\omega_0) \end{pmatrix} \quad (1.37)$$

Its absolute value is given by

$$|\vec{B}_{\text{eff}}| = \left[B_1^2 + \left(B_0 - \frac{\omega_{\text{rf}}}{\gamma_N} \right)^2 \right]^{1/2} = \frac{1}{\gamma_N} \left[\omega_1^2 + (\omega_0 - \omega_{\text{rf}})^2 \right]^{1/2} = \frac{\omega_{\text{eff}}}{\gamma_N} \quad (1.38)$$

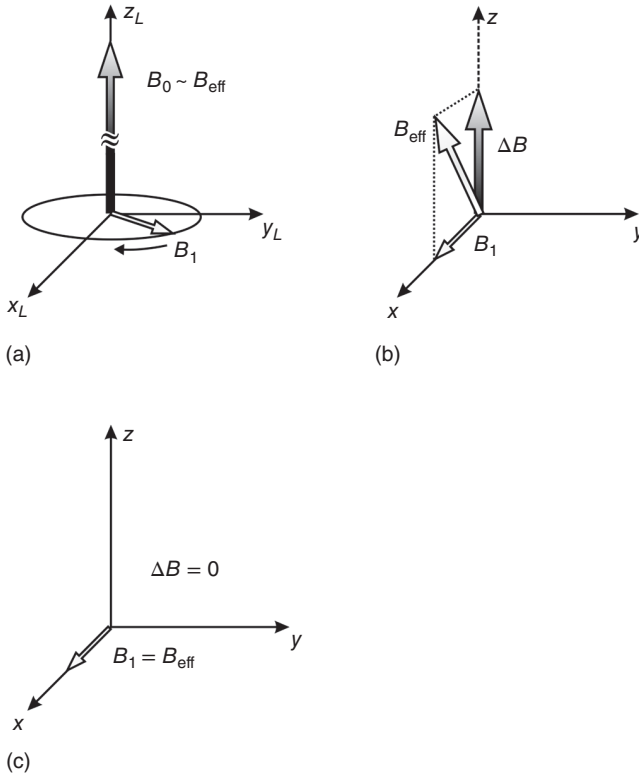


Figure 1.11 The effective magnetic field B_{eff} in the laboratory frame (a) and in the rotating frame for $\Delta B \neq 0$ (b) and $\Delta B = 0$ (c).

where the nutation frequencies $\omega_1 = \gamma_N B_1$ and $\omega_{\text{eff}} = \gamma_N B_{\text{eff}}$ describe the rotation frequency of the magnetization around B_1 (for $\omega_{\text{rf}} = \omega_0$) and B_{eff} (for $\omega_{\text{rf}} \neq \omega_0$), respectively.

After insertion of the above transformation in Eq. (1.35), the general *Bloch equations in the rotating frame* become

$$\begin{aligned} \frac{dM_x}{dt} &= (\omega_0 - \omega_{\text{rf}}) M_y - \frac{M_x}{T_2} \\ \frac{dM_y}{dt} &= -(\omega_0 - \omega_{\text{rf}}) M_x + \omega_1 M_z - \frac{M_y}{T_2} \\ \frac{dM_z}{dt} &= -\omega_1 M_y - \frac{M_z - M_0}{T_1} \end{aligned} \quad (1.39)$$

To follow the effect of the electromagnetic wave irradiation, the Bloch equations are solved for the “on-resonance” condition $\omega_{\text{rf}} = \omega_0$ and by neglecting the effects of the relaxation terms during RF irradiation. The following expressions for the magnetization components are obtained:

$$\begin{aligned} M_x(t) &= \text{const.} \\ M_y(t) &= M(0) \sin \omega_1 t \\ M_z(t) &= M(0) \cos \omega_1 t \end{aligned} \quad (1.40)$$

Here, $M(0)$ corresponds to the equilibrium magnetization M_0 . Accordingly, in the rotating frame, the magnetization is rotated around the x -axis in the y - z plane by a nutation angle

$$\theta_1 = \omega_1 t \quad (1.41)$$

For instance, after a $\pi/2$ rotation, the magnetization is along the y -axis, and no z -magnetization (longitudinal component) remains:

$$\theta = \frac{\pi}{2} \Rightarrow t_p = \frac{\pi}{2\gamma_N B_1} \quad (1.42)$$

Depending on the duration t_p and amplitude B_1 of irradiation, other directions of the magnetization in the y - z plane can be achieved. An RF pulse applied for a time necessary to rotate the magnetization by an angle θ on the y - z plane is commonly referred to as “ θ_x pulse.” The direction about which the magnetization rotates can also be expressed by an angle between 0° and 360° , representing the phase of the pulse. Conventionally, phases of 0° , 90° , 180° , and 270° respectively correspond to the x , y , $-x$, and $-y$ axes about which the magnetization rotates during the pulse. The rotation of the magnetization vector emphasizes the advantage of the transformation to the rotating frame. As illustrated in Figure 1.12, in the rotating frame, the magnetization directly rotates around the x -axis, while in the laboratory frame, both the high-frequency rotation of the Larmor precession and the oscillating RF field have to be considered yielding the spiral-like trajectory of the magnetization. In the following, unless otherwise stated, the movement of the magnetization vectors is always depicted in the rotating frame.

The above picture only holds strictly for the “on-resonance” condition. For all other cases with the “off-resonance” condition $\omega_{\text{rf}} \neq \omega_0$, the aforementioned effective magnetic field B_{eff} in the x - z plane has to be considered, around which the magnetization will rotate (Figure 1.13). In this connection, it should be kept in mind that B_1 is much smaller than B_0 , and therefore, it gives a significant contribution only if ω_{rf} approaches ω_0 . However, even for the “off-resonance” condition, it is justified to point the effective field along the x -axis, as long as the following condition holds:

$$B_1 \gg \Delta B = B_0 - \frac{\omega_{\text{rf}}}{\gamma_N} \quad \text{or} \quad \omega_1 \gg \omega_0 - \omega_{\text{rf}} = \Delta\omega \quad (1.43)$$

Later on, experiments will be discussed where the “off-resonance” condition is chosen on purpose (see, for instance, Lee–Goldburg decoupling, Chapter 5), i.e. the effective field is pointing along a well-defined direction in the x - z plane.

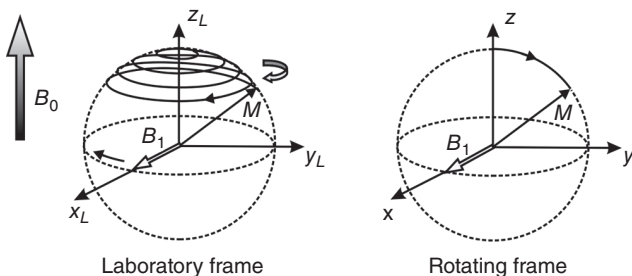


Figure 1.12 Time evolution of the magnetization under the effect of the RF field in the laboratory and rotating frames for $\Delta B = 0$.

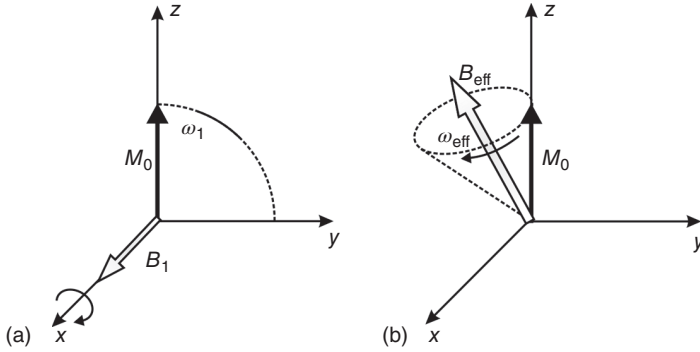


Figure 1.13 Time evolution of the magnetization under the effect of the RF field in the rotating frame in the cases $\Delta B = 0$ (a) and $\Delta B \neq 0$ (b).

After the application of the $\pi/2$ pulse with a B_1 component along the x -direction, the magnetization points along the y -direction with $\vec{M} = (0, M_0, 0)$. When the RF field is switched off, the magnetization evolves in the rotating frame in the presence of the static external magnetic field with

$$\vec{B}_{\text{eff}} = \begin{pmatrix} 0 \\ 0 \\ B_0 - \omega_{\text{rf}}/\gamma_N \end{pmatrix} = \begin{pmatrix} 0 \\ 0 \\ B_0 (1 - \omega_{\text{rf}}/\omega_0) \end{pmatrix} \quad (1.44)$$

The Bloch equations then become

$$\begin{aligned} \frac{dM_x}{dt} &= (\omega_0 - \omega_{\text{rf}}) M_y - \frac{M_x}{T_2} \\ \frac{dM_y}{dt} &= -(\omega_0 - \omega_{\text{rf}}) M_x - \frac{M_y}{T_2} \\ \frac{dM_z}{dt} &= -\frac{M_z - M_0}{T_1} \end{aligned} \quad (1.45)$$

which yield for the magnetization components in the rotating frame (Figure 1.14):

$$\begin{aligned} M_x(t) &= M(0) \sin [(\omega_0 - \omega_{\text{rf}}) t] e^{-t/T_2} = M_0 \sin(\Delta\omega t) e^{-t/T_2} \\ M_y(t) &= M(0) \cos [(\omega_0 - \omega_{\text{rf}}) t] e^{-t/T_2} = M_0 \cos(\Delta\omega t) e^{-t/T_2} \\ M_z(t) &= M(0) (1 - e^{-t/T_1}) = M_0 (1 - e^{-t/T_1}) \end{aligned} \quad (1.46)$$

It can be seen that the two transverse components M_x and M_y are modulated by the offset frequency $\Delta\omega = \omega_0 - \omega_{\text{rf}}$ and decay to zero with a time constant T_2 , the spin-spin relaxation time. The longitudinal magnetization M_z also approaches the equilibrium value M_0 with a characteristic time constant, denoted as the spin-lattice relaxation time T_1 .

The next step involves the back-transformation from the rotating frame to the laboratory frame. Since the same RF coil used for sample irradiation is employed for signal detection, the magnetization $M_{x,L}(t)$ has to be considered. After back-transformation, $M_{x,L}(t)$ contains a high-frequency term that, however, is removed by the admixture of a continuous-wave (c.w.) component of the same frequency ω_{rf} , as used during RF irradiation. From the resulting two signals, one with the sum and one with the difference of the mixed frequencies, the high-frequency

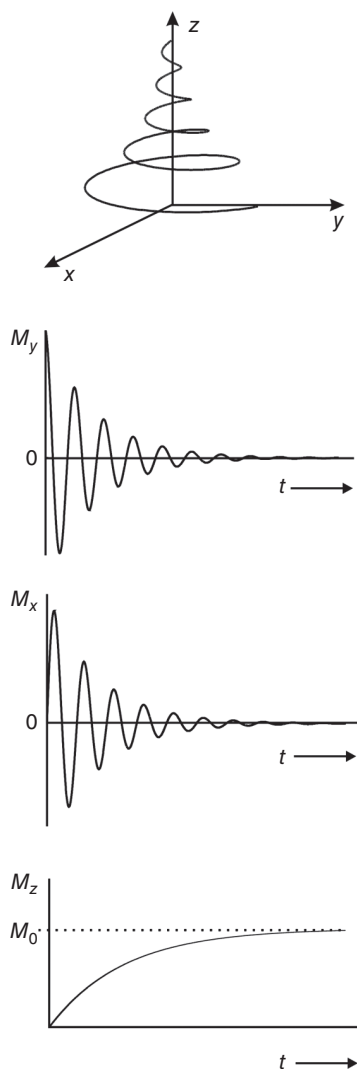


Figure 1.14 Time evolution of the magnetization and its components M_x , M_y , and M_z in the rotating frame after the application of a 90° pulse, following Bloch equation (Eq. (1.46)).

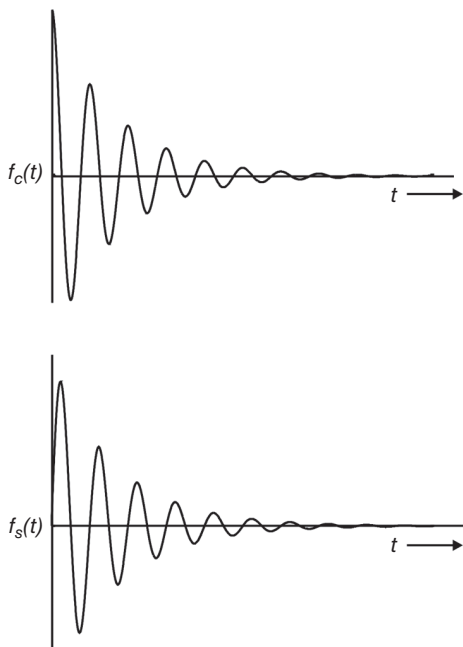
(summed) component is discarded, and only the difference signal in the audio frequency range remains.

For frequency selection, the admixture of the c.w. component is done twice (quadrature detection). The added c.w. components possess the same frequency ω but are phase-shifted by $\pi/2$. The resulting quadrature signals (Figure 1.15) are given by

$$\begin{aligned} f_C(t) &= A' \cos(\Delta\omega t) e^{-t/T_2} \\ f_S(t) &= A' \sin(\Delta\omega t) e^{-t/T_2} \end{aligned} \quad (1.47)$$

It is seen that apart from factor A' the signals are identical with the magnetization components $M_y(t)$ and $M_x(t)$ in the rotating frame, discussed earlier. That is, the

Figure 1.15 Quadrature signals $f_c(t)$ and $f_s(t)$ as a function of time.



NMR experiment, in fact, is done in the rotating frame, and the description in the rotating frame – as outlined earlier – offers several advantages.

The quadrature components are combined in the complex FID signal $f(t)$ by taking the component $f_c(t)$ as the real and the component $f_s(t)$ as the imaginary part

$$f(t) = f_c(t) + if_s(t) = A' [\cos(\Delta\omega t) + i \sin(\Delta\omega t)] e^{-t/T_2} \quad (1.48)$$

After Fourier transformation

$$F(\omega) = \int_0^{\infty} f(t) e^{-i\omega t} dt \quad (1.49)$$

the frequency spectrum is obtained (see Figure 1.16):

$$F(\omega) = A(\omega) + iD(\omega) \quad (1.50)$$

with the absorptive signal $A(\omega)$ in the real part and the dispersive signal $D(\omega)$ in the imaginary part (see Figure 1.17),⁴ as given by

$$A(\omega) = A' \frac{T_2}{1 + (\Delta\omega - \omega)^2 T_2^2}$$

⁴ It must be noted that this identification of the real and imaginary parts with, respectively, the absorptive and dispersive signals is too strict: depending on the experimental conditions, absorptive components may be present in the imaginary part and dispersive components in the real part. Nonetheless, this effect can be removed through a spectral processing procedure called constant phase correction, which consists of multiplying the spectrum by a term $\cos\zeta + i \sin\zeta$, with ζ the phase factor, the value of which has to be optimized to obtain a purely absorptive real spectrum.

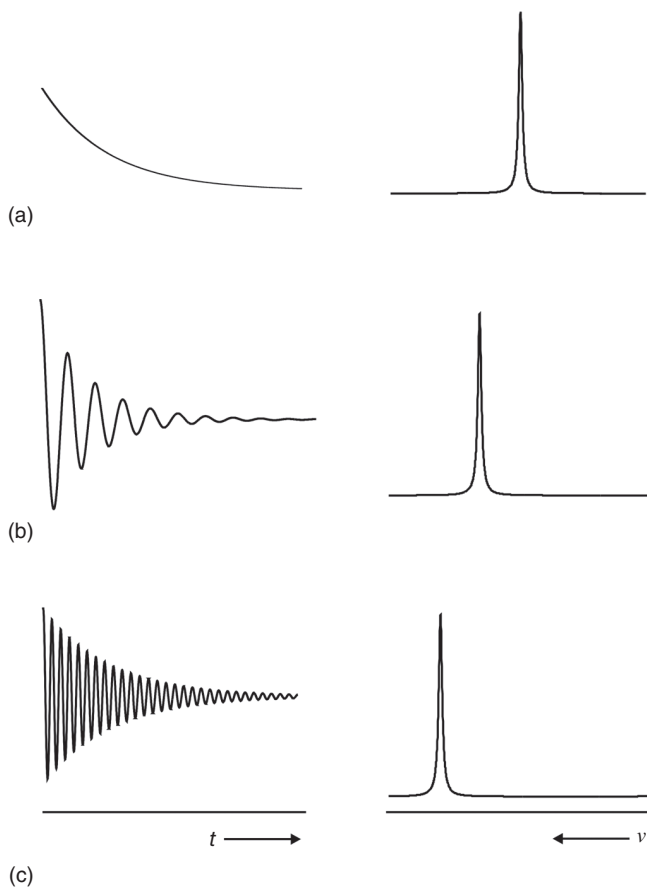


Figure 1.16 FIDs and corresponding frequency spectra obtained for (a) $\Delta\nu = 0$, (b) and (c) two different non-null $\Delta\nu$ values.

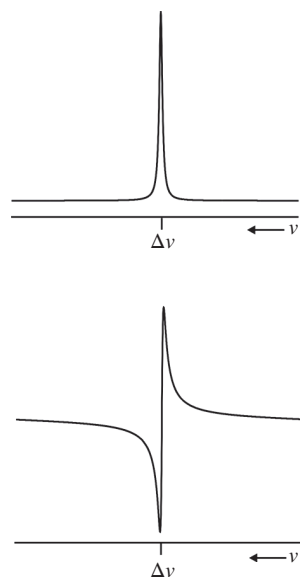
$$D(\omega) = A' \frac{T_2^2 (\Delta\omega - \omega)}{1 + (\Delta\omega - \omega)^2 T_2^2} \quad (1.51)$$

The absorption line is centered at $\omega = \Delta\omega$ (or, in linear frequency units, at $\nu = \Delta\nu$, being $\Delta\nu = \nu_0 - \nu = \omega_0/2\pi - \omega/2\pi$), and it is easy to see that its width at half the maximum height ($\Delta\omega_{1/2}$ or $\Delta\nu_{1/2}$) is inversely proportional to the spin–spin relaxation time T_2 , the characteristic decay time of the transverse magnetization

$$\Delta\omega_{1/2} = \frac{2}{T_2} \Rightarrow \Delta\nu_{1/2} = \frac{1}{\pi T_2} \quad (1.52)$$

It should be mentioned that, experimentally, the linewidth can be determined not only by the spin–spin relaxation time but also by magnetic field inhomogeneities. This implies that, in the above equations, an “effective” relaxation time T_2^* should be used instead of T_2 . Further below (Section 1.4.1), it will be shown how the true T_2 value can be measured experimentally.

Figure 1.17 Quadrature signals A and D (see Eq. (1.51)) as a function of frequency.



NMR pulse experiments are typically performed by summing up FID's from several identical experiments in order to improve the signal-to-noise ratio. In this context, the two relaxation times, T_2 and T_1 , are important quantities. The spin-spin relaxation time T_2 (or better T_2^*) determines the NMR linewidth, while T_1 determines the minimum time interval for repetition of the experiments during signal accumulation. Typically, the recycle delay should be in the order of five times T_1 to avoid saturation effects. It is important to note that the condition $T_2 \leq T_1$ holds.

At this point, we have to recall that all the above discussion concerning the effects of an RF pulse on nuclear magnetization was done under the assumption that the considered nucleus had a positive gyromagnetic ratio; precessions occurring in the opposite directions would have been obtained for nuclei with negative gyromagnetic ratios. This is quite inconvenient in practice, and it is instead useful to adopt a convention for which the effects of an RF pulse are independent of the type of nucleus. Unfortunately, as it is often the case, different conventions have been adopted within the NMR community. From now on, in this book, the following rule will be adopted: *independent from the type of nucleus, a " θ_ξ -pulse" indicates an RF pulse flipping the magnetization by a θ angle around the ξ axis in the sense established by the "right-hand" convention* (see Footnote 3). So, for instance, a 90°_x (or $\pi/2_x$) pulse applied on the magnetization directed along the z -axis will move the magnetization from the z -axis to the $-y$ -axis. It should be noted that this convention agrees with what is shown above only for nuclei with negative gyromagnetic ratios.

1.2.4 Populations and Coherences

Two important quantities were discussed above in connection with spin ensembles, namely, the population of the spin states and the various magnetization components. It has been shown that longitudinal magnetization in the z -direction arises

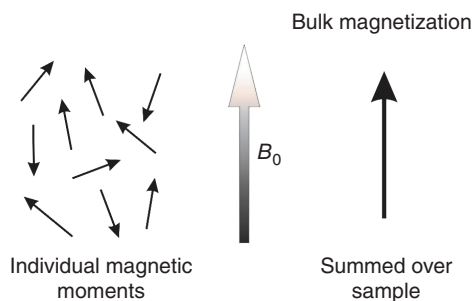


Figure 1.18 Orientation of the single magnetic moments and their sum at the thermal equilibrium in the presence of a strong external magnetic field.

from population differences between the spin states, while the existence of transverse magnetization requires a phase relationship among the individual magnetic moments that precess around the z -direction. It is useful to further develop this concept. At equilibrium, in the absence of external magnetic fields, the magnetic moments obviously distribute isotropically, giving no net magnetization. When the B_0 field is turned on along z , the magnetic moments preserve an almost isotropic distribution: actually, their components on the x - y plane are still isotropically distributed, but they have a slight tendency to be aligned toward $+z$ rather than $-z$, which causes the occurrence of a small net magnetization along z . The reason why the tendency to align toward $+z$ is only "slight" is due to the fact that the energy of interaction between the magnetic moments and B_0 is typically smaller than the thermal energy of the magnetic moments, allowing them to reorient almost freely. A scheme of this situation is given in Figure 1.18. In quantum mechanical terms, this means that, as previously stated, not only the Zeeman states but also all of their linear combinations are allowed (see Chapter 2). Restricting the discussion to spin-1/2 nuclei, the α and β states will have a 100% probability of obtaining $+1/2$ and $-1/2$, respectively, as a result of the "measurement" of I_z , while their linear combinations will have a certain probability of obtaining either $+1/2$ or $-1/2$, depending on the value of the coefficients in the linear combination. On the spin ensemble, however, the probability of measuring $+1/2$ is slightly higher than that of measuring $-1/2$, thus explaining again the occurrence of a net magnetization along $+z$. The fractional "population" of a Zeeman state must therefore be interpreted as the probability that the corresponding spin quantum number is found in the measurement of I_z .

Following the application of an RF pulse, the single magnetic moments and consequently the magnetization are tilted by a given angle, as demonstrated above. Moving the magnetization out of the z -axis toward the x - y plane consists of transforming the longitudinal into transverse magnetization or, in other terms, in transforming the difference of population into phase coherence of the spin vectors. When a $\pi/2$ -pulse is applied, the difference of population is canceled out (meaning that now, the probability of finding $+1/2$ and $-1/2$ for the measurement of I_z is exactly the same), and the phase coherence is maximized. On the other hand, the application of a π -pulse results just in the inversion of populations between the α and β states without the formation of any phase coherence in the x - y plane.

In general, the occurrence of a finite transverse magnetization arises from the presence of a phase coherence for the precession of the spins in adjacent spin states,

separated by $\Delta m = \pm 1$, also denoted as single quantum coherence (1Q coherence). Observable transverse magnetization is thus always accompanied by 1Q coherences of adjacent spin states. It should be mentioned that in coupled spin systems or for quadrupolar nuclei, multiple quantum (MQ) coherences (0Q, 2Q, 3Q coherence, ...) can also be achieved. Such coherences, however, cannot be detected directly. Rather, they can be followed in an indirect manner by the detection of the observable transverse magnetization as a function of the time evolution during which a particular MQ coherence exists. It will be shown later that the analysis of such MQ states can be used to extract valuable structural information (see Chapter 6).

1.3 Liquid-state NMR Spectroscopy: Basic Concepts

The importance of NMR spectroscopy for structural characterization is based on the fact that, apart from the direct interaction of the magnetic moments with the external magnetic field (nuclear Zeeman interaction), the nuclear spin states are further shifted or split up due to additional internal magnetic interactions, arising from the fact that the nucleus is not “bare” but it is surrounded by electrons and other nuclei of the same or of other molecules. These internal magnetic interactions include the shielding (chemical shift), the direct (or dipolar) and indirect (or J) spin–spin couplings, and, for nuclei with $I > 1/2$, the quadrupolar interaction, which are the most relevant interactions in diamagnetic systems. All these interactions have an isotropic and an anisotropic contribution, the latter of which depends on the orientation of the molecule (and of the molecular fragment to which the nucleus belongs) with respect to the external magnetic field B_0 . The internal interactions can be described through rank-2 tensors (see Chapter 3), the trace of which is proportional to the isotropic contribution. However, in liquid-state NMR spectroscopy, the molecules undergo fast isotropic reorientations which average out all anisotropic contributions, and only the isotropic part of the internal magnetic interactions remains visible in the spectra. As a result, in liquid-state NMR spectra, only two internal magnetic interactions are directly observable in the spectra, namely, (i) the chemical shift interaction and (ii) the indirect spin–spin coupling, since the trace of the dipolar and quadrupolar tensors is null.

1.3.1 Chemical Shift

The nuclei in an atom or in a molecule do not experience the same magnetic field that would be experienced by the bare nucleus. In particular, the nearby electrons within the atomic or molecular orbitals provide shielding (diamagnetic contribution) or deshielding (paramagnetic contribution) of the external magnetic field. Hence, the local magnetic fields at the nuclei are altered, which directly reflects the local chemical environments. The local field at a particular nucleus, B_{loc} , therefore differs from the applied external field B_0 by $B_{\text{ind}} = \sigma B_0$, the induced field (Figure 1.19), directed in the opposite direction, and given by

$$B_{\text{loc}} = B_0 - B_{\text{ind}} = (1 - \sigma) B_0 \quad (1.53)$$

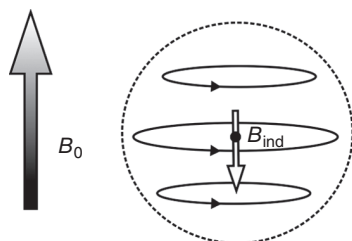


Figure 1.19 The local field B_{ind} induced by electrons in the presence of B_0 , altering the total magnetic field felt by the nucleus.

Here, σ is the shielding constant, which is a positive number much smaller than 1. If the local field is introduced in Eq. (1.9) for the potential energy of the spin states

$$E_{m_I} = -\hbar\gamma_N B_0 (1 - \sigma) I_z = -\hbar\gamma_N B_0 (1 - \sigma) m_I \quad (1.54)$$

then the transition frequency is given by

$$\omega = \gamma_N B_0 (1 - \sigma) \quad (1.55)$$

Again, the energy eigenvalues are obtained by solving the Schrödinger equation (Eq. (1.11)) with the appropriate spin functions and by inserting the shielding or chemical shift Hamiltonian

$$\hat{H} = -\hbar\gamma_N B_0 (1 - \sigma) \hat{I}_z \quad (1.56)$$

The shielding effect is registered for any NMR-active nucleus and represents a very important tool for structural characterization in chemistry. Since the resonance frequency depends on the external magnetic field strength, the field-independent chemical shift (δ) has been introduced, which is measured in parts per million (ppm) (Figure 1.20)

$$\delta = \frac{\omega - \omega_{\text{ref}}}{\omega_{\text{ref}}} \times 10^6 \text{ (ppm)} \quad (1.57)$$

where ω_{ref} is the resonance frequency of a reference compound, for which $\delta = 0$ ppm is conventionally assumed. For instance, in ^1H , ^{13}C , and ^{29}Si NMR experiments, $(\text{CH}_3)_4\text{Si}$, tetramethylsilane (TMS), is typically used. For the most common nuclei, the reference substances traditionally used are given in Table 1.3.

Although the above referencing has been used for many years and it is still in use in many laboratories, it should be mentioned that since 2001, International Union of Pure and Applied Chemistry (IUPAC) has recommended the use of a unified



Figure 1.20 Chemical shift δ or “ppm” scale and trends of shielding and frequency. The terms “low field” and “high field,” borrowed from the old continuous-wave techniques, are nowadays obsolete and are best avoided.

Table 1.3 Typical substances used as chemical shift references in liquid-state NMR for the most common nuclei.

Nucleus	Typical reference substance
^1H	1% $(\text{CH}_3)_4\text{Si}$ in CDCl_3
^{13}C	1% $(\text{CH}_3)_4\text{Si}$ in CDCl_3
^{19}F	neat CCl_3F
^{29}Si	1% $(\text{CH}_3)_4\text{Si}$ in CDCl_3
^{15}N	90% CH_3NO_2 in CDCl_3
^{31}P	85% H_3PO_4 in H_2O (D_2O)

scale for reporting chemical shifts of all nuclei, relative to the ^1H resonance of TMS (Harris et al. 2001).

As can be seen from Eq. (1.55), an increase in shielding (i.e. a larger σ value) reduces the resonance frequency and therefore the δ parameter. σ and δ are therefore related by the following equation

$$\delta = \frac{\sigma_{\text{ref}} - \sigma}{1 - \sigma_{\text{ref}}} \times 10^6 \text{ (ppm)} \approx (\sigma_{\text{ref}} - \sigma) \times 10^6 \text{ (ppm)} \quad (1.58)$$

where the approximate expression arises from $\sigma_{\text{ref}} \ll 1$.

The structural assignment by NMR chemical shifts is normally done with the help of empirical data from compounds of known structure. For instance, the resonance frequency of a ^1H nucleus varies remarkably, if it belongs to a methyl, methylene, methine, or hydroxyl group or to an aromatic ring. In addition, it is possible to predict chemical shift values for a particular chemical structure by means of quantum chemical methods (*ab initio* or DFT calculations).

In general, shielding contains two contributions due to the interactions of the electrons with the external magnetic field, a diamagnetic and a paramagnetic term:

$$\sigma = \sigma_{\text{dia}} + \sigma_{\text{para}} \quad (1.59)$$

The diamagnetic term σ_{dia} arises from motions of the ground state electrons in the orbitals, which induce an additional field component opposite to the external magnetic field (shielding) at the position of the nucleus. The diamagnetic contribution can be expressed by Lamb's formula

$$\sigma_{\text{dia}} = \frac{\mu_0 e^2}{3m_e} \int_0^\infty r \rho_e(r) dr \quad (1.60)$$

where $\rho_e(r)$, r , and m_e are the density of the electronic charge, the electron-nucleus distance, and the electron mass, respectively.

The paramagnetic term σ_{para} provides a magnetic field contribution in the same direction as the external magnetic field (deshielding effect), arising from electrons with a finite probability of being in excited electronic states. With the assumption that only s and p electrons are important, it can be shown by a linear combination of atomic orbitals – molecular orbitals (LCAO-MO) approach that σ_{para} depends

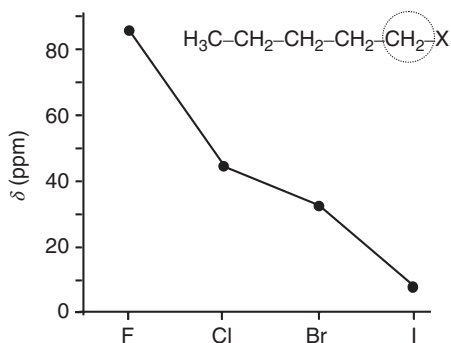


Figure 1.21 Example of the dependence of ^{13}C chemical shift on the electronegativity of bonded atoms.

on the average inverse cube distance of the valence p electrons from the nucleus ($\sigma_{\text{para}} \propto \langle r^{-3} \rangle$).

In order to better correlate chemical shift to molecular structure, it is advisable to separate the shielding constant into the following contributions:

$$\sigma = \sigma_{\text{dia}}(\text{local}) + \sigma_{\text{para}}(\text{local}) + \sigma_{\text{neighb}} + \sigma_{\text{hydr}} + \sigma_{\text{elect}} + \sigma_{\text{solv}} \quad (1.61)$$

The first two terms refer to local diamagnetic and paramagnetic shielding in the close vicinity of the nucleus. In particular, $\sigma_{\text{dia}}(\text{local})$ strongly depends on the electronic density which, for instance, is affected by bonded groups of different electronegativity (Figure 1.21). $\sigma_{\text{para}}(\text{local})$ strongly depends on the ease of exciting electrons to a higher electronic state. σ_{neighb} refers to contributions from remote groups with anisotropic susceptibility ($\text{C}=\text{O}$, $\text{C}=\text{C}$, $\text{C}=\text{N}$, ...) and from ring current effects in aromatic groups, also affecting the magnetic field experienced by the nucleus. For instance, the ring current enhances the local magnetic field of a nucleus located in the ring plane outside the aromatic unit (deshielding), while inside, directly above or below the ring, the local magnetic field is decreased (shielding), as shown in Figure 1.22. σ_{hydr} includes the effects of hydrogen bonding, for which deshielding of the ^1H resonance is observed with increasing hydrogen bond strength (Figure 1.23). σ_{elect} and σ_{solv} terms refer to contributions from electric fields of charged or polar groups and solvent effects, respectively.

The overall chemical shift changes as a function of chemical structure depending on the particular nucleus under consideration. As a general rule, the overall chemical shift range becomes larger in the periodic chart from top to bottom and from left to right. The former increase can be attributed to the increasing number of electrons, whereas the latter is a consequence of the atom contraction along with a reduction of the average nuclear-electron distance in the p-orbitals. Hence, the chemical shift range of ^1H (about 10 ppm) is considerably smaller than those of ^{13}C , ^{29}Si , or ^{19}F . Typical ^1H , ^{13}C , and ^{29}Si chemical shift ranges for selected functional groups are shown in Figure 1.24.

1.3.2 Indirect Spin-Spin Coupling and Spin Decoupling

The second important contribution to liquid-state NMR spectra arises from indirect spin-spin coupling, mediated via bonding electrons. The isotropic part of the

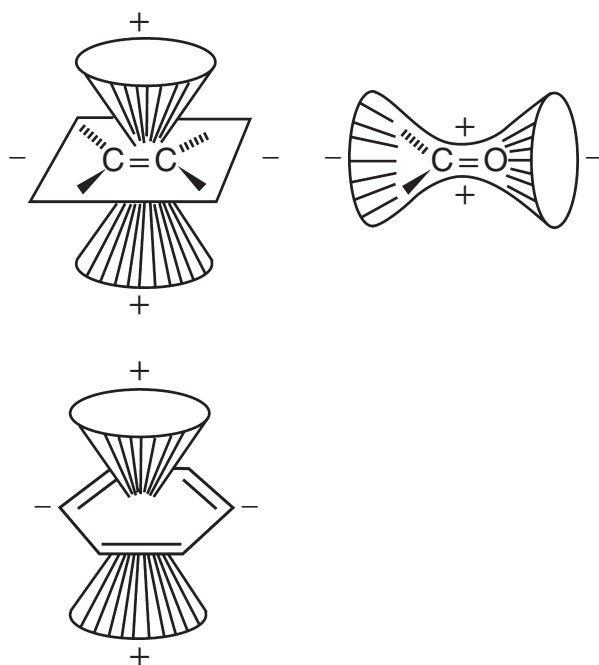
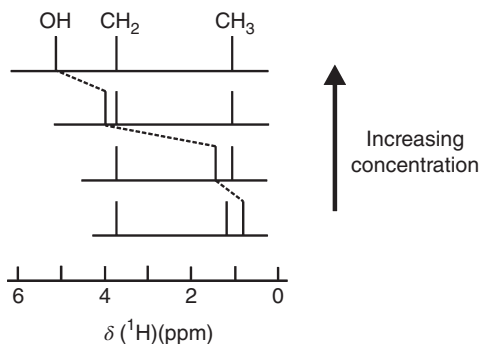


Figure 1.22 Shielding and deshielding effects (indicated with signs + and –, respectively) for C=C, C=O, and phenyl groups.

Figure 1.23 Trend of ^1H chemical shift of the hydroxyl proton in ethanol as a function of ethanol concentration in an apolar solvent. It is seen that as the concentration increases, i.e. when the average hydrogen bond strength increases, the chemical shift increases.



interaction, the only one surviving in a liquid, is a scalar (and no longer a tensorial) quantity: for this reason, the isotropic indirect spin–spin coupling is also called *scalar coupling*. The resonance frequency of a nucleus, coupled to other spins, also depends on the spin states of the coupled spins. In general, spin–spin coupling gives rise to a splitting of the Zeeman energy levels which, however, is much smaller (typically from few hertz to hundreds of hertz) than the overall chemical shift range discussed earlier. Furthermore, we commonly distinguish between interactions among the same (like spins) and different types of nuclei (unlike spins), denoted as homo- and heteronuclear spin–spin coupling, respectively, and between weak (first-order spectra) and strong coupling (higher-order spectra).

First-order spectra are found if the resonance frequency difference $\Delta\nu$ of the coupled spins is much larger than the scalar coupling constant J ($\Delta\nu \gg J$). Here, for a coupled two-spin system (AX system), the contribution to the energy of a spin state due to spin–spin coupling is obtained as a first-order perturbation of the full Hamiltonian (see Section 2.3.2) and contains the product of the magnetic spin quantum numbers m_A and m_X of the coupled nuclei A and X

$$E_{m_A m_X}^J = hJ_{AX} m_A m_X \quad (1.62)$$

multiplied by the scalar coupling constant J_{AX} . Together with the corresponding chemical shift contributions, one obtains

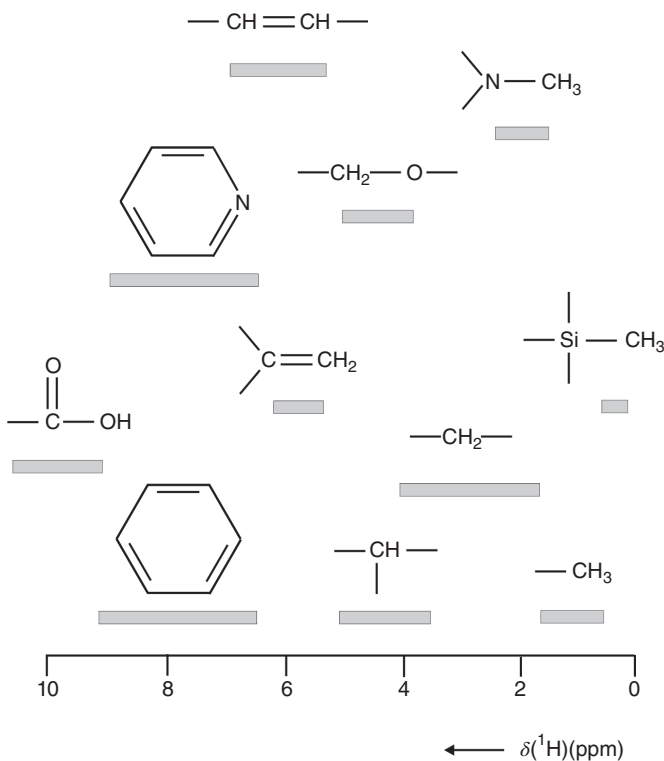
$$E_{m_A m_X} = -\hbar\gamma_A (1 - \sigma_A) B_0 m_A - \hbar\gamma_X (1 - \sigma_X) B_0 m_X + hJ_{AX} m_A m_X \quad (1.63)$$

For A transitions, the selection rules are

$$\Delta m_A = \pm 1 \quad \text{and} \quad \Delta m_X = 0 \quad (1.64)$$

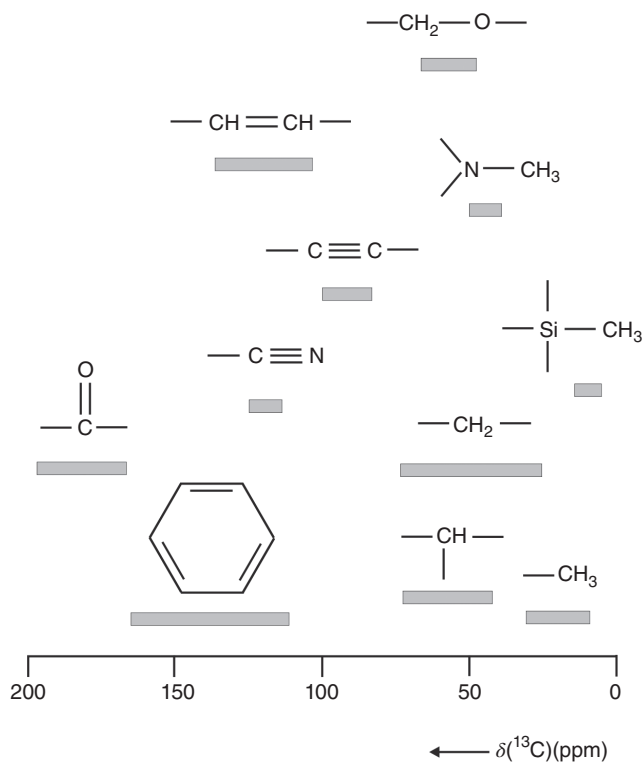
and for X transitions,

$$\Delta m_A = 0 \quad \text{and} \quad \Delta m_X = \pm 1 \quad (1.65)$$

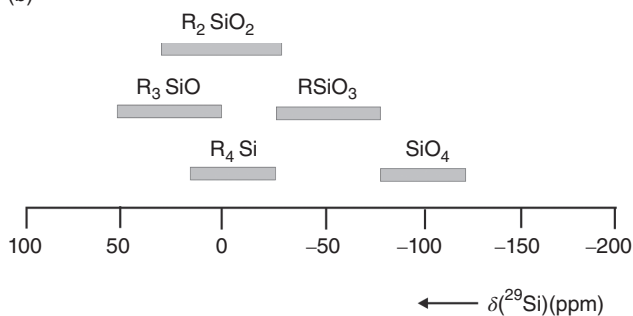


(a)

Figure 1.24 Typical ^1H (a), ^{13}C (b), and ^{29}Si (c) chemical shift ranges for selected functional groups.



(b)



(c)

Figure 1.24 (Continued)

Figure 1.25 depicts the corresponding energy diagram for two coupled nuclei with spin $1/2$ along with the expected NMR spectrum. It is seen that in the presence of spin-spin coupling, the A and X transitions split up giving rise to two lines, which are separated by the coupling constant J_{AX} . Examples from coupling to inequivalent and several equivalent nuclei with spin $1/2$ are shown in Figure 1.26. In the latter case, the line intensities can be predicted by Pascal's triangle. Similar NMR spectra are obtained if coupling to nuclei with spin larger than $1/2$ occurs, for which the above equations also hold. In general, it is found that for the weak coupling case, the

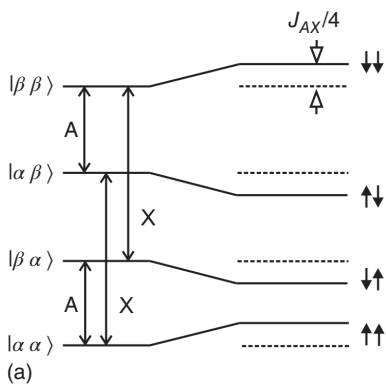
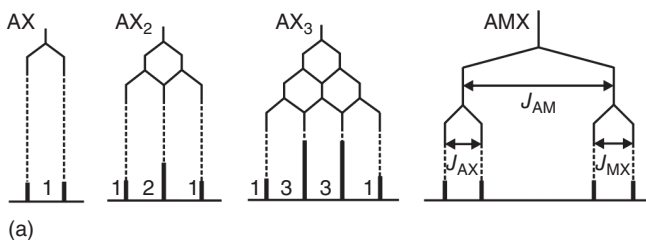
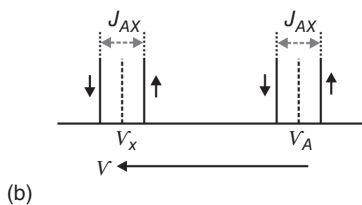


Figure 1.25 (a) Scheme of the transitions among energy levels for two spin-1/2 nuclei without (left) and with (right) scalar coupling (AX system). (b) Corresponding spectra without (dashed lines) and with (solid lines) scalar coupling. Close to each solid line, the spin state of the coupled nucleus is reported.



(b)

#	Line intensity			
0	1			
1	1			1
2	1	2	1	
3	1	3	3	1

Figure 1.26 (a) Examples of line splitting arising from J coupling in systems AX, AX_2 , AX_3 , and AMX. (b) The Pascal's triangle giving the intensity of each line of a multiplet generated by J coupling with a certain number of spin-1/2 equivalent nuclei.

eigenfunctions are given by simple products of the single spin functions, for example, for the AX case, by $|\alpha\rangle|\alpha\rangle$, $|\alpha\rangle|\beta\rangle$, $|\beta\rangle|\alpha\rangle$, $|\beta\rangle|\beta\rangle$ (more simply indicated as $|\alpha\alpha\rangle$, $|\alpha\beta\rangle$, etc.).

Higher-order spectra are obtained for strong spin coupling, where the difference of chemical shift between the coupled nuclei and the coupling constant J is of

comparable size. In this case, the full Hamiltonian

$$\hat{H} = -\sum_i \hbar\gamma_i B_0 (1 - \sigma_i) \hat{I}_{z,i} + \sum_{i<j} \hbar J_{ij} \hat{I}_i \cdot \hat{I}_j \quad (1.66)$$

has to be considered. For two strongly coupled spins (*AB* case), it becomes

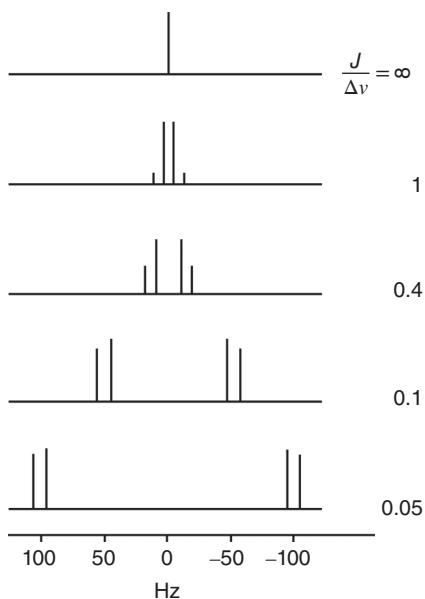
$$\hat{H} = -\hbar\gamma_A B_0 (1 - \sigma_A) \hat{I}_{z,A} - \hbar\gamma_B B_0 (1 - \sigma_B) \hat{I}_{z,B} + \hbar J_{AB} \hat{I}_A \cdot \hat{I}_B \quad (1.67)$$

That is – unlike the above weak coupling case, where only the *z* components are considered (first order correction) – for the higher-order spectra, also the *x*- and *y*-components of the spin vectors have to be taken into account in the coupling term. As a result, the simple product spin functions are no longer eigenfunctions, i.e. have to be mixed. In general, relatively complex NMR spectra arise that depend on the chemical shift difference of the coupled nuclei, $\Delta\nu$, and the *J* coupling (see Figure 1.27). The limiting cases for the *AB* spectra are the weak coupling case ($\Delta\nu \gg J$, see above) and the coupling of equivalent nuclei ($\Delta\nu \ll J$), the latter of which does not exhibit any signal splitting.

Indirect spin–spin coupling is transmitted via the electrons of the system, i.e. interactions between the nuclei and electrons of the molecules (Fermi contact interaction) as well as couplings between the various electron spins. Again, it is possible to predict spin–spin couplings by quantum mechanical methods that, however, are much more demanding than for chemical shift calculations.

The assignment of experimental spin–spin couplings again largely relies on empirical data. For instance, for one-bond couplings ($^1J_{\text{CH}}$ -couplings), it is found that the coupling constant increases linearly with the *s*-character of the carbon atomic orbital. As another example, for three-bond couplings ($^3J_{\text{HH}}$ in H–C–C–H

Figure 1.27 Spectra arising from *J* coupling between two like spin-1/2 systems as a function of the $J/\Delta\nu$ ratio. In all cases, $J = 10$ Hz.



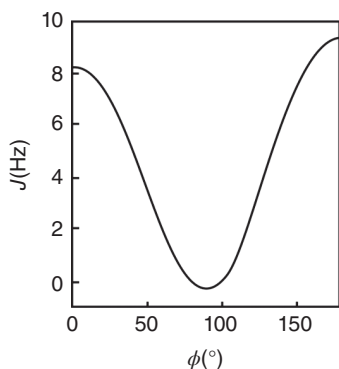


Figure 1.28 Dependence of the scalar coupling constant ${}^3J_{\text{HH}}$ from the dihedral angle ϕ as described by the Karplus relation, using typical values for parameters A and B .

fragments), the Karplus relation holds

$${}^3J_{\text{HH}} = A \cos^2 \phi + B \quad (1.68)$$

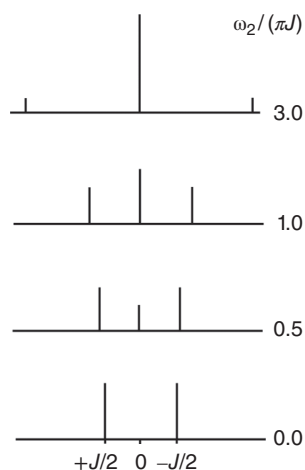
which describes the dependence of the coupling constant from the dihedral angle ϕ (Figure 1.28). A and B depend on substituents on C carbons. Additionally, A assumes different values for the two regions $0 \leq \phi \leq \pi/2$ and $\pi/2 \leq \phi \leq \pi$. Typical values are $B = -0.28$ Hz, $A = 8.5$ Hz for $0 \leq \phi \leq \pi/2$, and $A = 9.5$ Hz for $\pi/2 \leq \phi \leq \pi$. Similar expressions have been developed also for other three-bond coupling constants, such as ${}^3J_{\text{HH}}$ in HCOH or HCNH fragments.

Although spin–spin coupling contains valuable structural information, the corresponding NMR spectra may become very complex, and spin decoupling techniques are often employed to simplify the spectra. In order to remove heteronuclear spin–spin couplings, the signal of a particular type of nucleus is recorded, while all other or some of the other coupled nuclei are irradiated close to their respective Larmor frequencies. Quite elaborate techniques have been reported not only for heteronuclear but also for homonuclear decoupling. The simple heteronuclear double resonance experiment applied on an AX spin system consists of constant irradiation of the X nucleus by an RF field B_2 directed along the x -axis during the detection of the A nucleus. A more detailed description, even in theoretical terms, will be given in Chapter 4. For the moment, we limit the discussion to qualitatively understanding that decoupling arises from the orthogonality between the quantization axes for the A and X spins, respectively, along the B_0 (z -axis) and the B_2 direction (x -axis in the rotating frame). Due to the orthogonal orientation of the two quantization axes, the scalar product in the coupling term becomes zero, i.e. spin–spin coupling is removed. In Figure 1.29, it is shown how an increasing decoupling field B_2 affects the spectrum of an AX spin system.

1.3.3 Nuclear Spin Relaxation

Due to the small energy differences between the spin states, the probability for spontaneous transitions in NMR is practically negligible, and only stimulated spin transitions play a role. The influence of RF irradiation, discussed previously, results in a

Figure 1.29 Simulated spectra of the A nucleus in an AX system as a function of the ratio between decoupling power and J coupling constant while applying CW decoupling exactly on-resonance at the X nucleus.



disturbance of the equilibrium magnetization and the creation of observable transverse magnetization (from 1Q transitions $\rightarrow \Delta m_1 = \pm 1$). Spin relaxation describes the return of the spin system from a nonequilibrium state back to equilibrium. This involves in the most general case transitions between spin states and/or loss of phase coherence. Again, spin relaxation requires induced transitions due to the presence of magnetic field components fluctuating randomly in time at the various nuclei in the sample (i.e. incoherent radiation). Such fluctuating fields arise from various types of anisotropic magnetic interactions, which are modulated in time. For $I = 1/2$ nuclei, dipolar interactions, chemical shift anisotropy, and spin rotation⁵ (in order of decreasing importance) are the dominant contributions. For nuclei with $I > 1/2$, the quadrupolar interaction is normally dominant although the other aforementioned contributions may also play a role. The absolute values of these interactions are randomly altered with time, primarily by molecular reorientations, which give rise to different orientations of the molecules (or molecular fragments) with respect to the external magnetic field. Due to their stochastic nature, magnetic field fluctuations do not occur at a single frequency. Rather, they are characterized by a broad distribution of frequencies and, unlike the coherent excitations by RF pulses with only a transverse field component, possess magnetic field components in x -, y -, and z -direction. A qualitative discussion of relaxation effects can be done via the Bloch equations in the rotating frame by consideration of fluctuating B_x , B_y , and B_z components (Figure 1.30).

As for spin transitions caused by coherent RF fields, spin relaxation due to fluctuating transverse B_x - and B_y -components is accompanied by spin transitions, which become very efficient if fluctuations at frequencies in the order of the Larmor frequency possess a high probability. This is the *nonadiabatic* (non-secular) contribution to relaxation for the longitudinal (T_1 or spin-lattice relaxation) and transverse magnetization components (T_2 or spin-spin relaxation). In the case

⁵ The spin-rotation interaction is given by the coupling of the nuclear spin with the magnetic moment associated with the orbital angular momentum of the molecule.

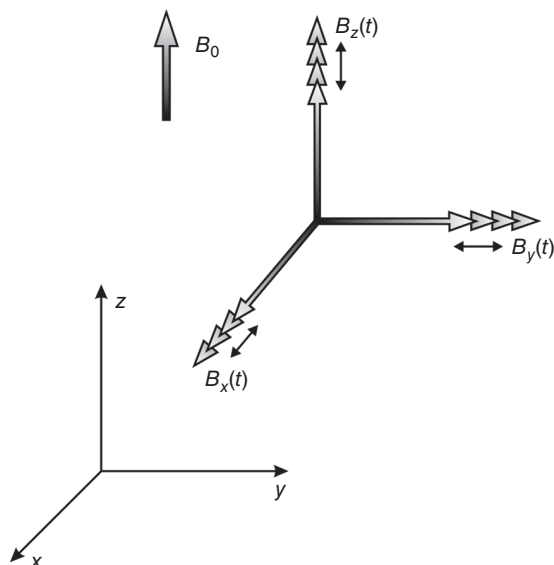


Figure 1.30 Fluctuation of B_x , B_y , and B_z components of the magnetic field at the nucleus due to the time modulation of local nuclear interactions caused by molecular motions.

of spin–lattice relaxation, the nonadiabatic contribution results in population changes until the equilibrium Boltzmann distribution is reached, i.e. energy transfer between the spin system and environment (=lattice) takes place. In the case of spin–spin relaxation, no net energy change is involved, and the induced spin transitions reduce the lifetimes of the spin states, which in turn affect the NMR linewidths and thus T_2 . For spin–spin relaxation, there is a second contribution due to the fluctuating B_z component. This *adiabatic* (secular) contribution causes no spin transitions. Rather, it varies the total magnetic field in z -direction, shifting the energy levels, hence increasing the linewidths, and affecting T_2 . Unlike the former high-frequency B_x and B_y contributions, the important part of the fluctuating B_z component is a zero-frequency contribution, which only affects T_2 .

In addition to T_1 and T_2 , describing the return to equilibrium of the longitudinal and transverse magnetization, respectively, in the absence of RF irradiation, a third relaxation time plays an important role in NMR, namely, the spin–lattice relaxation time in the rotating frame ($T_{1\rho}$), describing the return to equilibrium of the transverse magnetization during a time in which it is forced to stay aligned with a given axis of the x – y plane by a spin–lock irradiation.

Already in 1948, Bloembergen, Purcell, and Pound used a perturbation theory approach (“BPP theory”) and showed that the relaxation times can be expressed as a linear combination of spectral densities $J(\omega)$ that are a measure of the relative amount (or density) of fluctuating magnetic fields in a particular frequency range.

If spin relaxation is determined by several contributions, the total relaxation rate, i.e. the inverse of the corresponding relaxation time, is given by the sum of the individual contributions, i.e.

$$\frac{1}{T_1} = \sum_i \frac{1}{T_{1,i}}; \quad \frac{1}{T_2} = \sum_i \frac{1}{T_{2,i}}; \quad \frac{1}{T_{1\rho}} = \sum_i \frac{1}{T_{1\rho,i}} \quad (1.69)$$

The spectral density is related by the Fourier transformation

$$J(\omega) = \int_{-\infty}^{\infty} G(\tau) e^{-i\omega\tau} d\tau \quad (1.70)$$

to the autocorrelation function $G(\tau)$

$$G(\tau) = \langle f(t)^* f(t + \tau) \rangle \quad (1.71)$$

where $f(t)$ is the spatial part of the time-dependent nuclear spin interaction and the brackets $\langle \rangle$ indicate an ensemble average at any particular moment or the average over a long time for a single spin (ergodic hypothesis). Bloembergen, Purcell, and Pound based their analysis on the Debye theory, describing the fast isotropic reorientational motion of a rigid sphere, which results in a decaying exponential form for the autocorrelation function

$$G(\tau) = e^{-\frac{|\tau|}{\tau_c}} \quad (1.72)$$

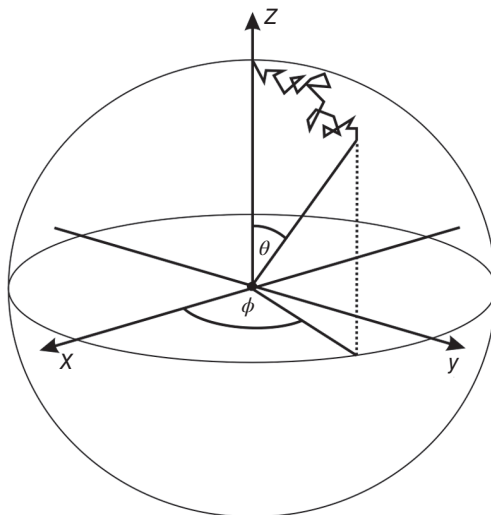
Here, τ_c is the motional correlation time, which is a time constant for the fluctuations of the magnetic field components inducing spin relaxation. If isotropic Brownian motion of a molecule is considered to be the source for the fluctuating fields, then τ_c is given by the time it takes to change on average the orientation on the surface of a sphere by 1 radian (Figure 1.31).

By Fourier transformation of $G(\tau)$ in Eq. (1.72), a Lorentzian form for the corresponding spectral density is obtained:

$$J(\omega) = \frac{2\tau_c}{1 + \omega^2\tau_c^2} \quad (1.73)$$

The autocorrelation function characterizes the magnetic field fluctuations, as briefly described in the following (Figure 1.32). For fast fluctuating magnetic fields (on a timescale much shorter than the inverse Larmor frequency), the autocorrelation function exhibits a fast memory loss, as expressed by a fast decaying function

Figure 1.31 Representation of a random reorientational motion: τ_c can be seen as the time for which $\theta = 1$ radian.



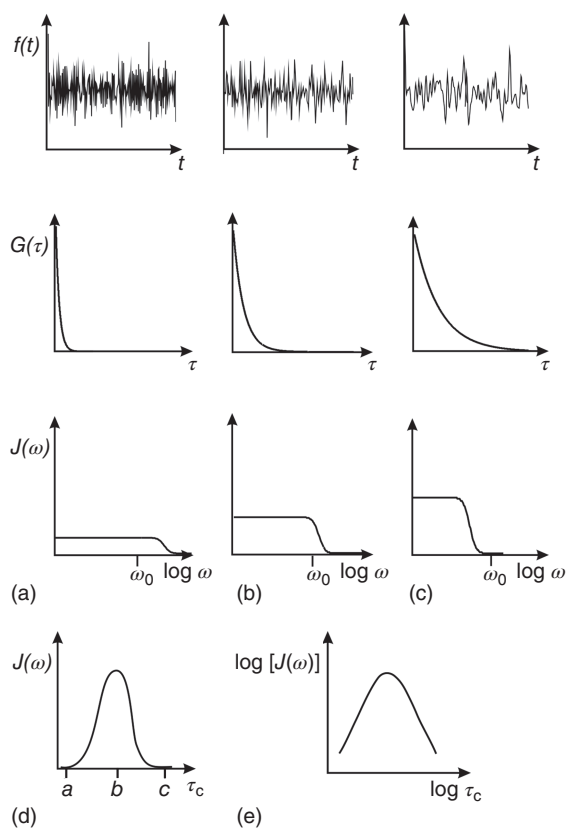


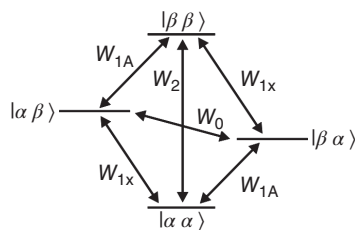
Figure 1.32 Schematic representation of $f(t)$, $G(\tau)$, and $J(\omega)$ in three different cases: (a), (b), and (c), corresponding to motions fast ($\omega_0 \tau_c \ll 1$), intermediate ($\omega_0 \tau_c \approx 1$), and slow ($\omega_0 \tau_c \gg 1$) with respect to the Larmor frequency. In (d) and (e), the linear and logarithmic plots of $J(\omega)$ as a function of the correlation time of the motion τ_c are reported, respectively. The cases (a), (b), and (c) are indicated on the abscissa of (d), highlighting the occurrence of a maximum of $J(\omega)$ for the intermediate motion.

$G(\tau)$ and thus a short correlation time τ_c . At the other extreme, for slow fluctuating magnetic fields (timescale much longer than the inverse Larmor frequency), the function $G(\tau)$ reflects a longer memory, the correlation time τ_c becomes longer, and $G(\tau)$ decays more slowly. In Figure 1.32, the normalized spectral density functions, which become broader with decreasing τ_c , are also shown. Moreover, due to the normalization of the spectral density – for the intermediate τ_c – a maximum value for the spectral density at the Larmor frequency ω_0 is observed, which in turn results in efficient spin relaxation (i.e. a minimum T_1 value; see below).

From these examples, it is quite obvious that the autocorrelation function/spectral density pair is similar to the FID/NMR spectrum one, both being Fourier pairs. FID and NMR spectrum are characterized by the spin–spin relaxation time T_2 (“phase-memory time”), while for the autocorrelation function and the spectral density, the correlation time τ_c plays the same role.

Figure 1.33 depicts the spin states of a heteronuclear coupled two-spin system (AX, $I = 1/2$ spins) along with various transitions responsible for spin relaxation: (i) single quantum (W_{1A} and W_{1X}), (ii) double-quantum (W_2), and (iii) zero-quantum transitions (W_0). It can be shown that the relaxation rates $1/T_1$ and $1/T_2$ depend on the various transition rates that are connected with the spectral density functions. With

Figure 1.33 Scheme of the spin states and the possible zero-, single-, and double-quantum transitions for a heteronuclear coupled two-spin 1/2 system.



the assumption that spin relaxation is only determined by heteronuclear dipolar coupling of an isolated pair of nuclei, the transition rates become

$$\begin{aligned} W_0 &= \frac{1}{20} C^2 J(\omega_X - \omega_A) \\ W_{1A} &= \frac{3}{40} C^2 J(\omega_A) \\ W_{1X} &= \frac{3}{40} C^2 J(\omega_X) \\ W_2 &= \frac{3}{10} C^2 J(\omega_X + \omega_A) \end{aligned} \quad (1.74)$$

which depend on the spectral densities $J(\omega_i)$

$$J(\omega_i) = \frac{2\tau_c}{1 + \omega_i^2 \tau_c^2} \quad (1.75)$$

and the dipolar coupling constant C

$$C = \frac{\mu_0}{4\pi} \gamma_A \gamma_X \hbar \frac{1}{r_{AX}^3} \quad (1.76)$$

It can be shown that the relaxation times of nucleus A are given by

$$\begin{aligned} \frac{1}{T_{1A}^{\text{DDU}}} &= \frac{1}{20} C^2 [J(\omega_X - \omega_A) + 3J(\omega_A) + 6J(\omega_X + \omega_A)] \\ &= \frac{1}{10} C^2 \left[\frac{\tau_c}{1 + (\omega_X - \omega_A)^2 \tau_c^2} + \frac{3\tau_c}{1 + \omega_A^2 \tau_c^2} + \frac{6\tau_c}{1 + (\omega_X + \omega_A)^2 \tau_c^2} \right] \end{aligned} \quad (1.77)$$

$$\frac{1}{T_{2A}^{\text{DDU}}} = \frac{1}{40} C^2 [4J(0) + J(\omega_X - \omega_A) + 3J(\omega_A) + 6J(\omega_X) + 6J(\omega_X + \omega_A)] \quad (1.78)$$

$$\frac{1}{T_{1\rho A}^{\text{DDU}}} = \frac{1}{40} C^2 [4J(2\omega_1) + J(\omega_X - \omega_A) + 3J(\omega_A) + 6J(\omega_X) + 6J(\omega_X + \omega_A)] \quad (1.79)$$

where the index DDU indicates that these expressions refer to relaxation times arising from the modulation of the dipolar interaction between unlike nuclei.

Analogous expressions can be derived for all the other interactions, and in particular, those due to the dipolar interaction between two like spin-1/2 nuclei are given

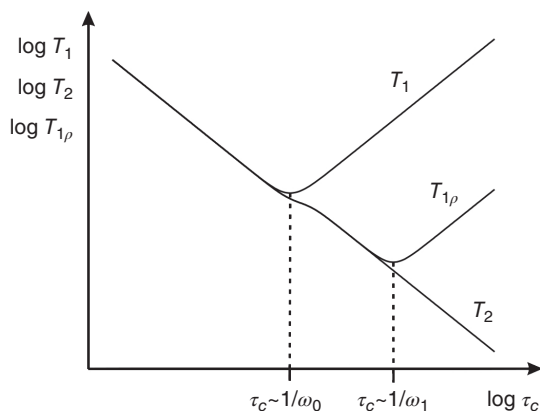


Figure 1.34 Logarithmic plot of the theoretical trends of T_1 , T_2 , and $T_{1\rho}$ vs. τ_c . The curves are calculated assuming that the relaxation arises from the modulation, due to a single isotropic motional process, of the homonuclear dipolar interaction between two spins-1/2, on the basis of Eqs. (1.80)–(1.82), assuming the BPP expression of the spectral densities given in Eq. (1.75).

by

$$\frac{1}{T_{1A}^{\text{DDL}}} = \frac{3}{20} C^2 [J(\omega_A) + 4J(2\omega_A)] \quad (1.80)$$

$$\frac{1}{T_{2A}^{\text{DDL}}} = \frac{3}{40} C^2 [3J(0) + 5J(\omega_A) + 2J(2\omega_A)] \quad (1.81)$$

$$\frac{1}{T_{1\rho A}^{\text{DDL}}} = \frac{3}{40} C^2 [3J(2\omega_1) + 5J(\omega_A) + 2J(2\omega_A)] \quad (1.82)$$

Theoretical relaxation curves are shown in Figure 1.34, where T_1 , $T_{1\rho}$, and T_2 are plotted as a function of the motional correlation time τ_c . From the above equations, it is obvious that spin–lattice relaxation becomes most efficient at about the Larmor frequency ($\omega_0^2 \tau_c^2 \approx 1$), as expressed by a pronounced minimum. In a quite similar way, the $T_{1\rho}$ curve exhibits a minimum at around the nutation frequency ω_1 ($\omega_1^2 \tau_c^2 \approx 1$). Due to the additional zero-frequency term $J(0)$ for spin–spin relaxation, a continuous decrease of T_2 is observed with increasing correlation time up to the limit for the applicability of the BPP theory (i.e. $T_1, T_2, T_{1\rho} > \tau_c$).

In these diagrams, the left part, before the T_1 minimum, refers to the “extreme narrowing” region with very fast molecular motions in media of low viscosity ($\omega_0^2 \tau_c^2 \ll 1$), where $T_1 = T_{1\rho} = T_2$. The right side, beyond the T_1 minimum, refers to slow molecular motions with correlation times on a timescale being longer than the inverse of the Larmor frequency, reflecting media of high viscosity ($\omega_0^2 \tau_c^2 \gg 1$). Here, T_1 and T_2 deviate, and $T_2 < T_1$. It is thus obvious that spin relaxation represents an important tool for extracting information about molecular mobility.

1.3.4 Nuclear Overhauser Effect

Spin relaxation is also responsible for the NOE in coupled spin systems. In the steady-state NOE experiment, an intensity change (signal increase or decrease) is observed for one of the coupled spins, while the other spin is continuously irradiated with a weak RF field for some time. Such steady-state NMR experiments

are therefore mainly applied for signal enhancement in heteronuclear coupled spin systems (for instance, ^{13}C NMR signal enhancement during ^1H irradiation).

In Figure 1.35, the steady-state NOE experiment is schematically depicted for a pair of dipolar coupled spin-1/2 nuclei (AX) with the same sign of γ . In the first step, both X transitions are irradiated until saturation of these transitions is achieved (nonequilibrium Boltzmann distribution). At the same time, spin relaxation takes place involving all possible transitions (zero quantum, W_0 ; single quantum, W_1 ; double quantum, W_2). Here, two cases are distinguished. When $W_2 > W_0$, the signal of spin A is enhanced as compared to the reference experiment without X-RF irradiation (positive NOE). When $W_0 > W_2$, a decrease in the signal intensity of the A nucleus (negative NOE) is observed. Hence, after sufficiently long irradiation, the X transitions are saturated, and the nonequilibrium populations are partially compensated by spin relaxation. That is, the spin system approaches a stationary state with a constant population difference between the levels involved in the A transitions, which is essential for the theoretical description.

The NOE is best described by the Solomon equations, which are rate equations for the changes of the spin state populations $n_{\alpha\alpha}$, $n_{\beta\beta}$, $n_{\alpha\beta}$, and $n_{\beta\alpha}$ with time. As an example, the expression for $dn_{\alpha\alpha}/dt$ is given by

$$\frac{dn_{\alpha\alpha}}{dt} = - (W_{1A} + W_{1X} + W_2) (n_{\alpha\alpha} - n_{\alpha\alpha}^0) + W_2 (n_{\beta\beta} - n_{\beta\beta}^0) + W_{1A} (n_{\beta\alpha} - n_{\beta\alpha}^0) + W_{1X} (n_{\alpha\beta} - n_{\alpha\beta}^0) \quad (1.83)$$

where $n_{\alpha\alpha}^0$, $n_{\beta\beta}^0$, $n_{\beta\alpha}^0$, and $n_{\alpha\beta}^0$ are the corresponding equilibrium populations and the rates W_{1A} , W_{1X} , W_2 , and W_0 are defined in Figure 1.33. Similar equations are found for the time dependence of the populations $n_{\beta\beta}$, $n_{\alpha\beta}$, and $n_{\beta\alpha}$. The solution of the Solomon equations is done for the aforementioned stationary state conditions, i.e. a constant population difference between the levels involved in the A transitions and a zero population difference for those of the X transitions (since they are saturated). This yields for the ratio of the signals S_A^* and S_A for the A nucleus with and without X-saturation, respectively,

$$\frac{S_A^*}{S_A} = 1 + \frac{\gamma_X}{\gamma_A} \frac{W_2 - W_0}{W_0 + 2W_{1A} + W_2} = 1 + \eta \quad (1.84)$$

where η is the NOE enhancement.

In Figure 1.36, it is shown how the enhancement η changes with the correlation time of the motion τ_c . In general, these curves depend on the particular coupled spin system. It can be seen how, for coupled nuclei with the same sign of γ , the maximum NOE enhancement is obtained in the extreme narrowing limit $\omega_0^2 \tau_c^2 \ll 1$ (positive NOE). Under this condition, the spectral densities are all equal to $2\tau_c$ (Eq. (1.75)), $W_2 > W_0$, and the ratio S_A^*/S_A becomes (see Eq. (1.74))

$$\frac{S_A^*}{S_A} = 1 + \frac{\gamma_X}{2\gamma_A} = 1 + \eta_{\max} \quad (1.85)$$

Therefore, the A-signal is enhanced by $\gamma_X/2\gamma_A$ (about 2 for a ^{13}C - ^1H pair).

For slower motions, $\omega_0^2 \tau_c^2 \gg 1$, and $W_2 < W_0$ (negative NOE), which results in a decrease of η . It must be noted that an opposite trend is obtained when the two

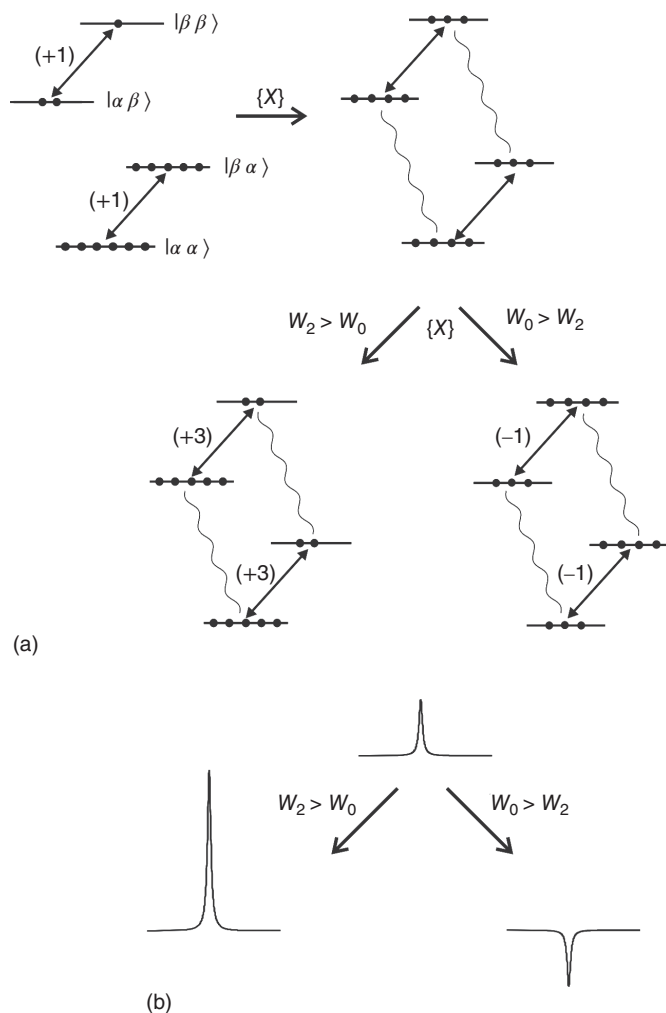
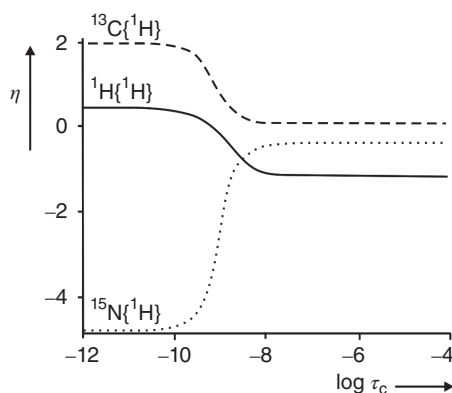


Figure 1.35 Schematic representation of the NOE experiment for a dipolar coupled AX spin system. (a) Equilibrium populations and allowed A transitions (left) and effect of the irradiation of X transitions, leading to their saturation and consequently altering the equilibrium populations (right). (b) Effects of spin relaxation in the two cases of positive ($W_2 > W_0$) and negative ($W_0 > W_2$) NOE, leading, respectively, to increased and decreased population differences between the spin states involved in A transitions, with consequent effects on NMR signals. The number of nuclei populating the different states, indicated as full circles on the corresponding energy levels, is just intended to give a greatly simplified scheme and is by no means representative of the true populations obtained from the Boltzmann distribution. The numbers in parentheses next to the A transitions indicate the differences in population referred to in this simplified scheme.

Figure 1.36 Trends of NOE enhancement η vs the correlation time of the motion, τ_c , for ^1H , ^{13}C , and ^{15}N nuclei coupled to ^1H nuclei.



coupled nuclei have gyromagnetic ratios with opposite signs, as in the case $^{15}\text{N}-^1\text{H}$ (see Figure 1.36).

1.4 Liquid-state NMR Spectroscopy: Some Experiments

1.4.1 Relaxation Experiments

Unlike other spectroscopies, relaxation phenomena are very important in NMR spectroscopy.

Previously, the spin–lattice (T_1) and spin–spin (T_2) relaxation times were introduced that denote the time constants for return of the longitudinal and transverse magnetization components, respectively, to their equilibrium values. On the basis of the previous discussion, spin–lattice relaxation is thus accompanied by changes of the spin state populations, involving an energy transfer between the spin system and the local neighborhood (energy relaxation). For spin–spin relaxation, no net change of the spin state populations occurs. Rather, the individual spins lose their phase relationship (coherence) resulting in an enhanced entropy, i.e. entropy relaxation occurs.

The spin–lattice relaxation time T_1 can be determined either by the inversion recovery or the saturation recovery method (Figures 1.37 and 1.38). In the first experiment, the magnetization is inverted by a π pulse toward the $-z$ -direction, and the return of the magnetization to the equilibrium value is measured as a function of the relaxation interval τ by a $\pi/2$ read pulse, which creates observable transverse magnetization. The saturation recovery experiment is almost identical, except that the longitudinal magnetization is zeroed at the beginning of the experiment by a $\pi/2$ or a series of $\pi/2$ pulses. For the signal evolution as a function of the relaxation interval τ , the equation

$$\frac{dM_z}{d\tau} = -\frac{M_z(\tau) - M_0}{T_1} \quad (1.86)$$

has to be solved. For the inversion recovery experiment, one obtains

$$M_z(\tau) = M_0 [1 - 2 \exp(-\tau/T_1)] \quad (1.87)$$

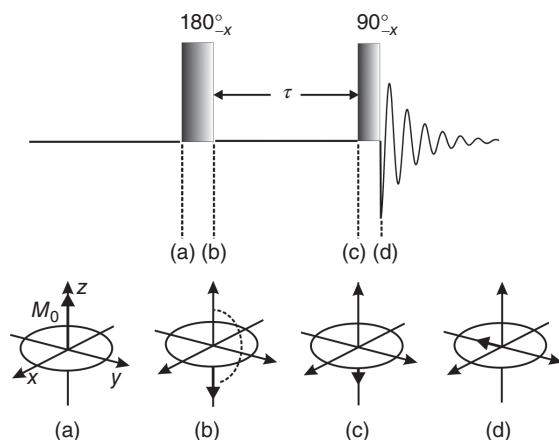


Figure 1.37 Inversion recovery pulse sequence and the corresponding evolution of the magnetization. In an experiment for the measurement of T_1 , a series of spectra is recorded at different values of τ .

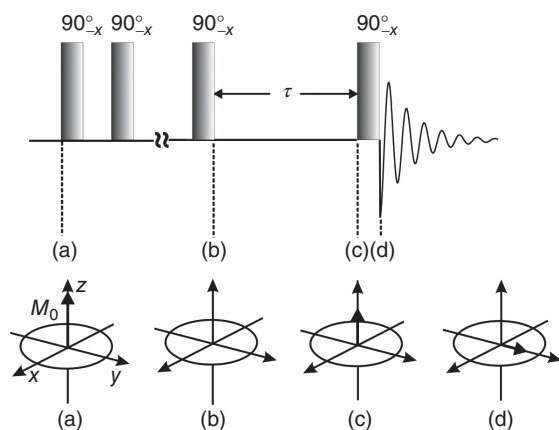


Figure 1.38 Saturation recovery pulse sequence and the corresponding evolution of the magnetization. In an experiment for the measurement of T_1 , a series of spectra is recorded at different values of τ .

or

$$\ln [M_0 - M_z(\tau)] = \ln (2M_0) - \tau/T_1 \quad (1.88)$$

Likewise, for the saturation recovery experiment, the expression

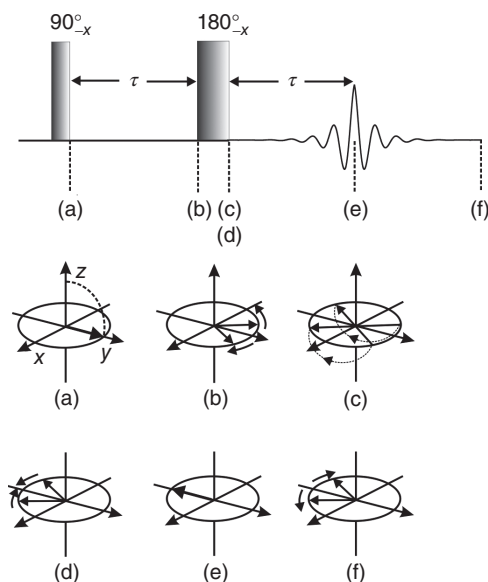
$$\ln [M_0 - M_z(\tau)] = \ln M_0 - \tau/T_1 \quad (1.89)$$

is derived. Hence, from a semilogarithmic plot of $M_0 - M_z(\tau)$ vs the interval τ , the relaxation time T_1 can be easily obtained. One of the advantages of the inversion recovery experiment is that the dynamic range of the signal intensity is double that of the saturation recovery experiment. Moreover, in the inversion recovery experiment, T_1 can be approximately derived from the zero-crossing of the magnetization, for which the condition

$$M_z(\tau) = 0 \rightarrow \tau = T_1 \times \ln 2 \approx 0.69 \times T_1 \quad (1.90)$$

holds. The main advantage of the saturation recovery experiment is that one starts at zero magnetization, i.e. it is not necessary to wait between successive experiments until the magnetization is fully recovered. The recycle delay between successive experiments can be therefore much shorter than for the inversion recovery

Figure 1.39 Pulse sequence for the standard spin-echo experiment. The corresponding evolution of the magnetization shows the dephasing due to field inhomogeneity and the subsequent rephasing to give an echo for a spin not experiencing J coupling, for an on-resonance RF irradiation, and for a virtually infinite T_2 (the refocused magnetization is equal to the equilibrium one). In an experiment for the measurement of T_2 , a series of FIDs are recorded at different values of τ .



experiment. However, in contrast to inversion recovery, in this experiment, undesired transverse magnetization may be created (as echoes) that must be zeroed, so it requires that $T_2^* < \tau' \ll T_1$, where τ' is the interpulse spacing in the initial train of saturation pulses. The condition $T_2^* \ll T_1$ is usually met in solids, while in liquids, the shortening of T_2^* is possibly achievable using PFG.

The spin-spin relaxation time T_2 is experimentally accessible by the spin-echo experiments. The standard spin-echo experiment is depicted in Figure 1.39, where its effect is also shown for isolated spins. Although it is the result of a substantial modification by Carr and Purcell (1954) of the original Hahn echo (Hahn 1950), this experiment is still called the “Hahn echo,” but in this book, we will refer to it as “standard spin-echo experiment.” Here, after the first $\pi/2$ pulse, the spin vectors fan out due to the slightly different local fields experienced by the nuclei. There are two main reasons for these different local fields: (i) the local (typically dipolar) couplings experienced by the spins and their time dependence and (ii) the inhomogeneity of the external magnetic field. While the first effect, related to the true T_2 , is incoherent and therefore irreversible, the field inhomogeneity effect is coherent, and therefore, it can be completely reversed by the application of a π pulse at time τ . Hence, the spins start to rephase, and a spin-echo signal is formed at time 2τ . The refocusing effect of a 180° pulse on magnetization components precessing at different constant frequencies around B_0 is better detailed in Figure 1.40. Analysis of the echo intensity $A(2\tau)$ as a function of 2τ yields the true T_2 without contribution from field inhomogeneities

$$|A(2\tau)| = M_0 \exp(-2\tau/T_2) \quad (1.91)$$

Hence, a semilogarithmic plot of the echo height $A(2\tau)$ against 2τ yields a slope of $1/T_2$. It should be noted that, when an ensemble of like-nuclei is considered,

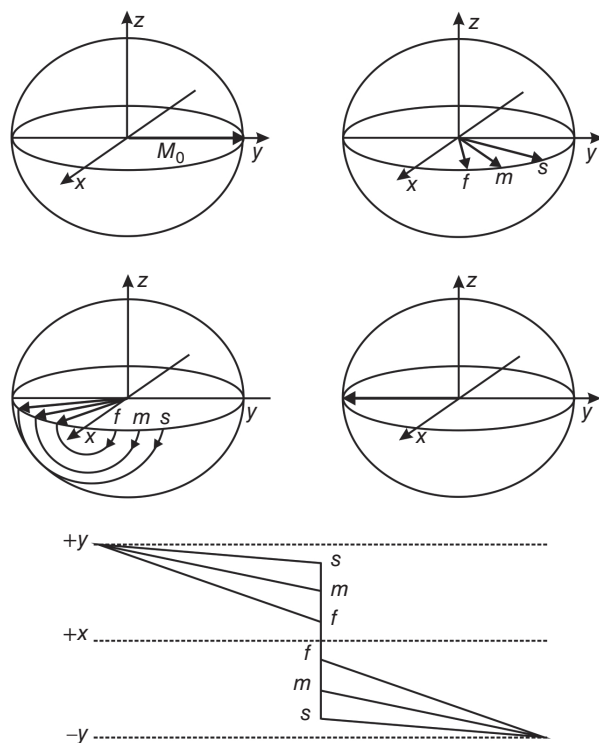


Figure 1.40 Refocusing effect of a 180°_{-x} pulse on three different magnetization components precessing at different frequencies (f = fast, m = medium, s = slow) around B_0 .

the refocusing effect also applies to chemical shift differences in the same fashion described above for field inhomogeneity.

If homonuclear scalar coupled nuclei are present the situation is more complex. π pulse (i.e. a short RF pulse which affects all coupled spins in the sample) not only flips the spins around the B_1 field direction, but also interconverts the α and the β spins (Figure 1.41, top). Therefore, the spins do not completely rephase after 2τ , and the echo height and phase depends not only on the τ value but also on the scalar J coupling. The resulting echo modulation is exploited, for instance, in 2D NMR spectroscopy (J , δ -experiment) to separate isotropic chemical shift and J coupling contributions.

Application of the standard spin-echo experiment to heteronuclear coupled spin systems yields the same spin-echo phenomenon as for uncoupled spins (Figure 1.41, bottom). That is, if the π pulse is only irradiated at the A nuclei, then only the observed spins are affected (A spins). However, if π pulses are applied on both the A and the X spins (Figure 1.42), then the same echo modulation effect is found as for homonuclear J -coupled spins.

It should be noted that translational diffusion effects may limit the application of the standard spin-echo technique, since during the experiment, a given nucleus would experience different locations and therefore different local fields

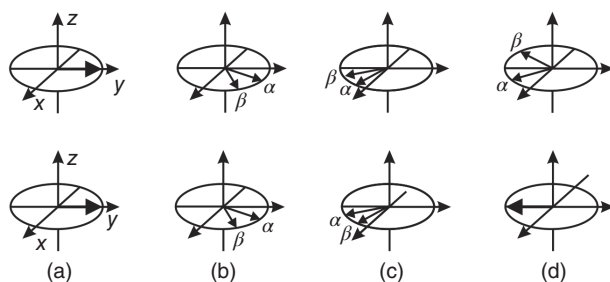
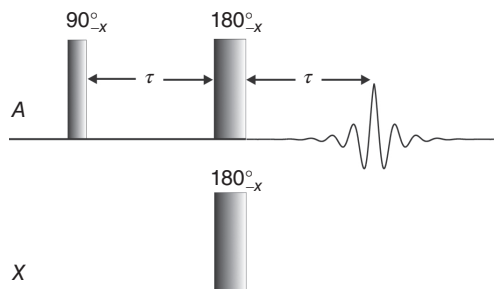


Figure 1.41 Effect of the standard spin-echo experiments on the magnetization components of two J -coupled spin-1/2 nuclei. The cases of a homo- (AB) and heteronuclear (AX) spin pairs are shown at the top and bottom, respectively. Two components are shown, arising each from about a half of the nuclei A, either coupled to α or β spin states of nucleus B (X). The situation is described at different times of the pulse sequence: (a) after the initial 90°_{-x} pulse, (b) after a subsequent evolution time τ , (c) soon after the 180°_{-x} pulse, and (d) after an additional evolution time τ . It should be noted that the 180° pulse flips the A magnetization components around x (exchanging the order of the slow and the fast components) when heteronuclear coupling is present, and therefore, it generates refocusing of the two components. In the case of homonuclear coupling, the 180° pulse also acts on nucleus B, inverting its α and β states and therefore canceling out the flipping effect and not generating any refocusing of the two components.

Figure 1.42 Standard spin-echo experiment modified in order to remove the refocusing effect on heteronuclear J coupling: the introduction of a 180° pulse on X nuclei, simultaneous to that on A nuclei, causes the pulse sequence to act like in the case of homonuclear J coupling (top).



due to the magnetic field inhomogeneity. This problem can be overcome by the Carr–Purcell–Meiboom–Gill (CPMG) experiments that are extensions of the standard spin-echo experiment. The initial $\pi/2$ pulse is followed by a train of π pulses, separated by time delays of 2τ (Figure 1.43). The intensity of the CPMG echo signal (including the diffusion term) after the n th π pulse is given by

$$|A(t = 2n\tau)| = M_0 \exp(-t/T_2) \exp\left(-\frac{1}{3}\gamma_N^2 G^2 D \tau^2 t\right) \quad (1.92)$$

Here, G and D are the spatial magnetic field gradient and the diffusion constant, respectively. It must be noted that G can be ordinarily considered as a measure of the magnetic field inhomogeneity, but a known field gradient can also be introduced with the purpose of measuring D . From Eq. (1.92), it can be seen that the diffusion effect is minimized if a sufficiently short pulse spacing τ is applied.

Spin–lattice relaxation times in the rotating frame, $T_{1\rho}$, can be obtained using the spin–lock experiment (Figure 1.44). Here, after an initial $(\pi/2)_{-x}$ pulse, the phase of the RF field is shifted by $\pi/2$. The RF field now points along the y -direction,

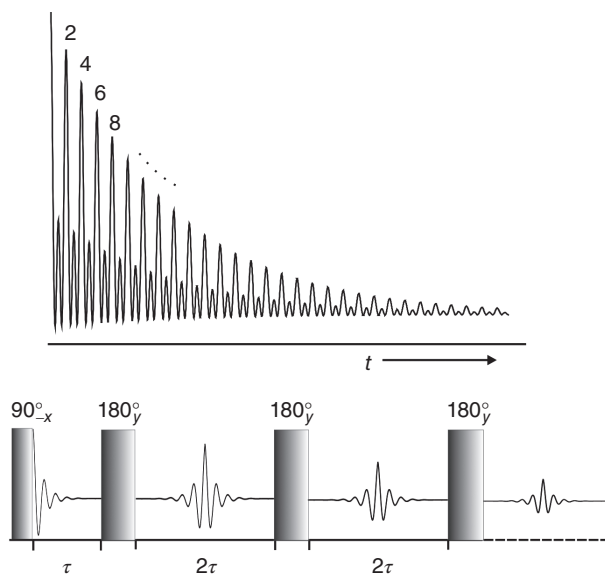


Figure 1.43 Carr–Purcell–Meiboom–Gill (CPMG) pulse sequence and trend of the echo signal as a function of time. The number above the echoes is the time expressed as “times τ .”

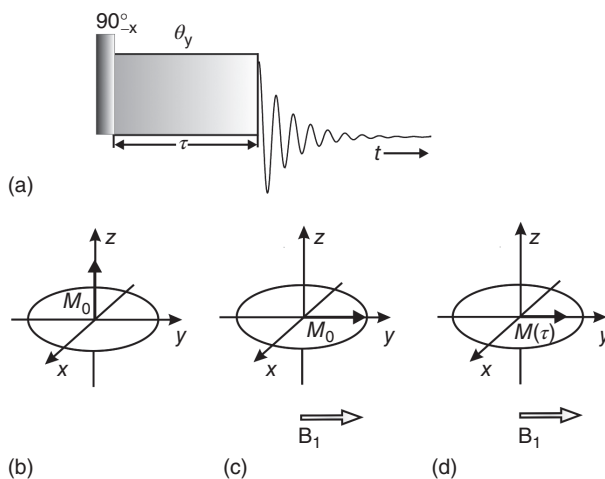


Figure 1.44 (a) Spin–lock pulse sequence and the corresponding evolution of the magnetization. The situation is described at different times of the pulse sequence: (b) at the equilibrium, (c) soon after the initial 90° pulse, (d) after a spin–lock time τ . In an experiment for the measurement of $T_{1\rho}$, a series of FIDs is recorded at different values of the spin–lock time τ .

i.e. the direction of the magnetization, and is left on for a variable time τ . During this period, the magnetization relaxes under the influence of the B_1 field (relaxation in the rotating frame), which is considerably weaker than the external B_0 field. The relaxation time $T_{1\rho}$ describes the magnetization decay for this experiment, which is given by

$$A(\tau) = M_0 \exp(-\tau/T_{1\rho}) \quad (1.93)$$

Thus, from a semilogarithmic plot of $A(\tau)$ against τ , the relaxation time $T_{1\rho}$ is derived.

1.4.2 Insensitive Nuclei Enhanced by Polarization Transfer

Another possibility for signal enhancement in heteronuclear coupled spin systems is the *insensitive nuclei enhanced by polarization transfer* (INEPT) experiment. The basic double resonance experiment is depicted in Figure 1.45. Here, the τ value during the first spin-echo part of the experiment is chosen so that $\tau = 1/4J_{AX}$, which results, after the first evolution time, in a 90° out-of-phase orientation of the magnetization components $M_X^{A\alpha}$ and $M_X^{A\beta}$ of the X nuclei coupled with the A spins in the α and β states, respectively. The simultaneous π_x pulses cause a flip of the two magnetization components about the x -axis as well as their exchange. Therefore, after a subsequent evolution for a time τ , the two magnetization components become aligned along the x -axis but out of phase by 180° , behaving similarly to what was previously observed for the spin-echo sequence of Figure 1.42. The $(\pi/2)_y$ pulse on the X nuclei then rotates both magnetization vectors along the z and $-z$ -directions, which is the same as a population inversion for one of the X transitions (Figure 1.46a). This population inversion gives rise to intensity changes for the A transitions, which is then read out by a $(\pi/2)_x$ pulse on the A channel (Figure 1.46b). The overall signal enhancement factor of the INEPT experiment is

$$\eta = \frac{\gamma_X}{\gamma_A} \quad (1.94)$$

which is a factor of two larger than the maximum enhancement factor due to the NOE effect. A further important difference between the two techniques is that the NOE enhancement relies on incoherent (stochastic) processes from relaxation effects, which strongly depend on the underlying relaxation mechanism. In contrast, the INEPT experiment is based on a coherent process, i.e. magnetization transfer due to RF pulse excitation, which is completely independent of relaxation effects and therefore of general applicability.

1.4.3 2D NMR Spectroscopy

Two-dimensional and multidimensional (nD) NMR techniques are extensions of the conventional 1D FT NMR experiment, realized by inserting a second or more time intervals prior to the detection of the NMR signal. Hence, in 2D NMR spectroscopy, the NMR signal (time domain t_2) is detected as a function of another time interval, t_1 , introduced in the pulse sequence. The general scheme for a 2D NMR experiment

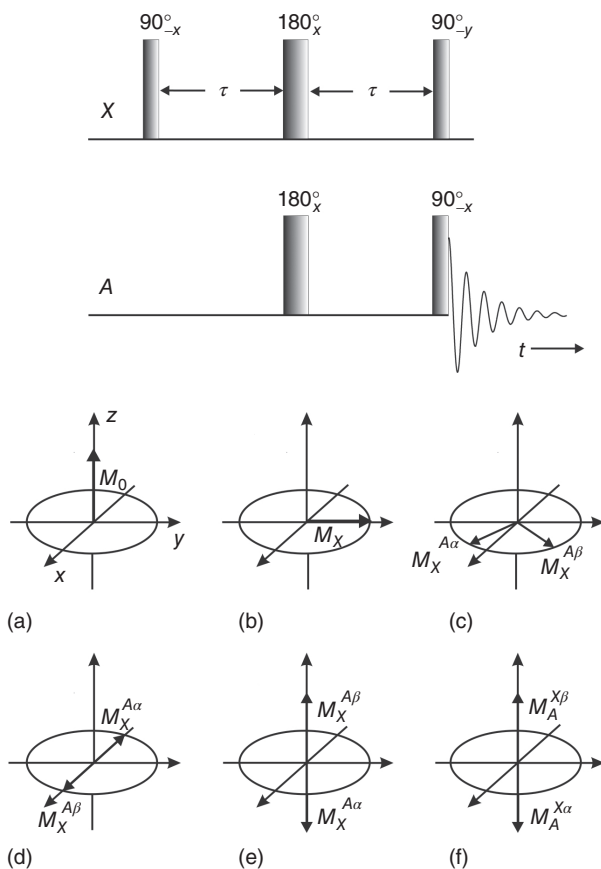


Figure 1.45 Pulse sequence of the basic double resonance INEPT experiment and the corresponding evolution of the X and A magnetization components, with $\gamma_X > \gamma_A$. The situation is described: (a) at equilibrium; (b) after the first 90°_{-x} pulse on the X-channel, (c) after the first evolution time τ , (d) after the two simultaneous 180° pulses that reflect the two magnetization vectors with respect to the xz plane and, at the same time, exchange the two magnetization vectors $M_X^{A\alpha}$ and $M_X^{A\beta}$, and after the subsequent evolution time τ resulting in a 180° -phase separation between the two magnetization vectors, now aligned along $-x$ and $+x$, respectively; (e, f) after the 90°_{-y} on the X-channel that brings $M_X^{A\beta}$ and $M_X^{A\alpha}$ along $+z$ and $-z$, respectively, causing a population inversion between the states $|\alpha\alpha\rangle$ and $|\alpha\beta\rangle$, equivalent to a hypothetical 180° pulse on the sole $M_X^{A\alpha}$ magnetization vector, and a consequent alteration of $M_A^{X\alpha}$ and $M_A^{X\beta}$, as shown in (f) and in Figure 1.46. The effect of the final 90° pulse on A-channel is that of transforming the latter longitudinal magnetization vectors into transverse, measurable ones, and it is better understood if thought of as applied soon after the experimentally simultaneous 90° pulse on the X-channel.

thus includes periods for preparation, evolution, and detection of the magnetization, as schematically depicted in Figure 1.47a. In the first period, the spin system is “prepared” into a defined state by one or a series of RF pulses. This is followed by the evolution period (t_1), during which the spin system evolves in the presence of a particular spin Hamiltonian. Finally, the detection period (t_2) requires the formation of

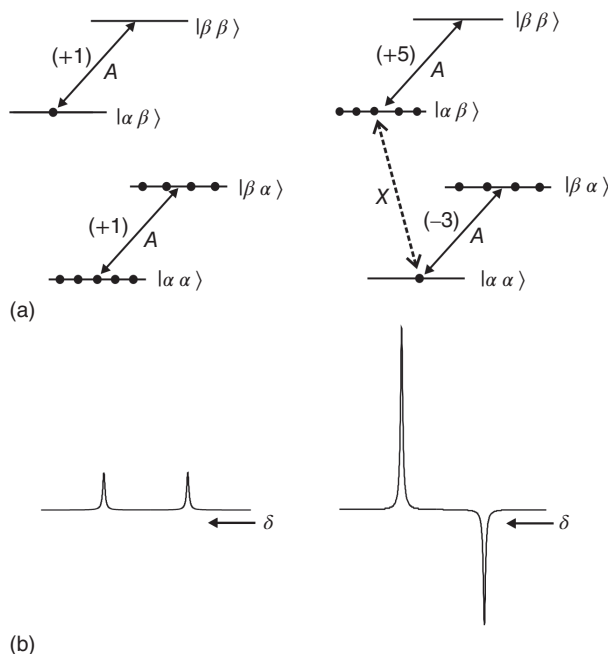
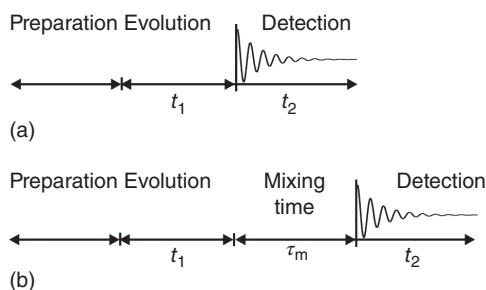


Figure 1.46 Scheme of the INEPT experiment for a J -coupled AX spin system. (a) Equilibrium populations and allowed A transitions (left) and populations after the application of the INEPT experiment (right). (b) Spectrum of the nucleus A corresponding to the two situations described in (a).

Figure 1.47 General schemes of pulse sequences for 2D experiments, (a) without and (b) with a mixing time.



transverse magnetization that is then recorded as a function of t_1 . In some cases, the general scheme is extended by an additional mixing interval (Figure 1.47b), as, for instance, in the nuclear Overhauser effect spectroscopy (NOESY) experiment.

The resulting two-dimensional data set $S(t_1, t_2)$ is firstly Fourier transformed with respect to t_2 , which yields NMR spectra $S(t_1, \omega_2)$ as a function of t_1 . A second FT along t_1 provides the 2D NMR spectrum $S(\omega_1, \omega_2)$, usually given in a contour representation (Figure 1.48). In the most general case, 2D NMR spectra consist of mixed absorptive and dispersive signals that give rise to additional line broadening. Several procedures have been proposed from which pure absorptive 2D NMR spectra with a reduced linewidth and better resolution are obtained.

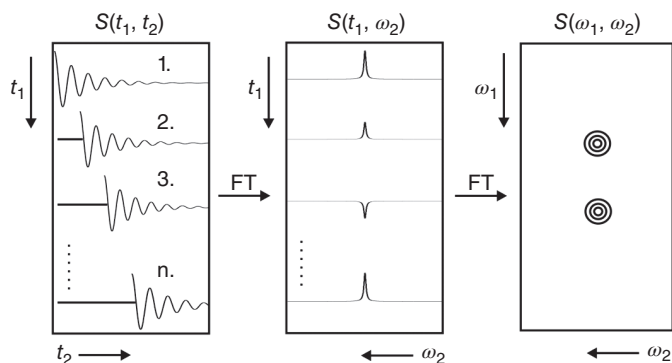


Figure 1.48 Effects of the double Fourier transformations applied to $S(t_1, t_2)$ to obtain a 2D spectrum, typically represented in the form of a contour plot.

The first proposed 2D NMR experiment was the homonuclear COSY (*correlation spectroscopy*) experiment with a simple pulse sequence given by $(\pi/2)-t_1-(\pi/2)-t_2$ (Figure 1.49). During the COSY experiment, magnetization transfer occurs between those coupled-like nuclei that have a sufficiently large homonuclear scalar coupling. As a result, 2D NMR spectra are observed which provide the connectivities between the nuclear spins in the investigated molecules. Along the diagonal, the normal 1D NMR spectrum is found, while the cross-peaks connect the resonances of scalar coupled nuclei, which are close neighbors in the molecular structure. Hence, from the

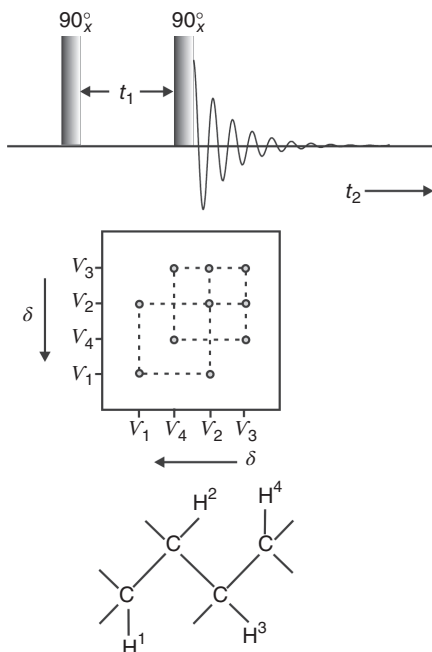


Figure 1.49 COSY experiment: pulse sequence and scheme of a 2D spectrum highlighting cross-peaks connecting signals of scalar coupled nuclei (in the example, three-bond ^1H nuclei).

COSY experiment, the signals of nuclei belonging to directly bonded structural units can be assigned.

Similar experiments for heteronuclear scalar coupled spin systems are the *heteronuclear correlation* (HETCOR) experiments. Here, the cross-peaks in the 2D NMR spectrum indicate those resonances of the A and X spins (for instance, ^1H and ^{13}C or ^1H and ^{29}Si , etc.) that are connected by a direct chemical bond. Several variants of this experiment are reported in the literature: as an example, in Figure 1.50, two pulse sequences are reported, based on direct and inverse detection of X nuclei. The first provides A–X decoupling in both dimensions (A decoupling in the X dimension and vice versa) through an INEPT-type mechanism combined with continuous RF irradiation on the A channel during acquisition on X. The second, better known as *heteronuclear multiple quantum coherence* (HMQC), exploits zero- and double-quantum coherences and consists in the acquisition in the A dimension during X decoupling (inverse detection).

The NOESY experiment, based on the three-pulse sequence depicted in Figure 1.51, again relies on magnetization transfer. Here, after the second $\pi/2$ pulse, the magnetization is stored along the $+z$ or $-z$ -axis. During the following mixing time, the exchange of magnetization takes place through relaxation effects in a dipolar coupled spin system. As a result, again, cross-peaks arise that connect the signals undergoing dipolar interaction. Dipolar coupling is a through-space interaction and therefore provides structural information that is complementary to the scalar (through-bond) spin–spin coupling information obtained from the COSY experiment.

Finally, in the incredible *natural abundance double-quantum transfer experiment* (INADEQUATE) (Figure 1.52), employed in ^{13}C NMR spectroscopy, homonuclear double-quantum coherence is created by the first three pulses. During the variable delay t_1 , the double-quantum coherence evolves, and it is indirectly detected through the signal modulations for the FID signal as a function of t_1 . In the INADEQUATE spectrum, the double-quantum frequencies are along the ω_1 -axis, while the conventional spectrum is along the ω_2 axis. Pairs of cross-peaks parallel to the ω_2 -axis indicate signals involved in a homonuclear scalar spin–spin coupling. The INADEQUATE experiment is thus a valuable analytic tool for the determination of the connectivity in the carbon framework of organic molecules.

Finally, it should be emphasized that numerous other 2D and multidimensional experiments have been proposed that also can be used for structural characterization. Their applicability strongly depends on the system under investigation and the structural question to be solved.

1.4.4 Chemical Exchange

Exchange is a ubiquitous phenomenon in NMR. It will be clear in the following chapters how the chemical shift observed in solution-state spectra arises from the averaging effect of the fast “exchange” between all different molecular orientations, each originally corresponding to a different chemical shift value. Moreover, it will be

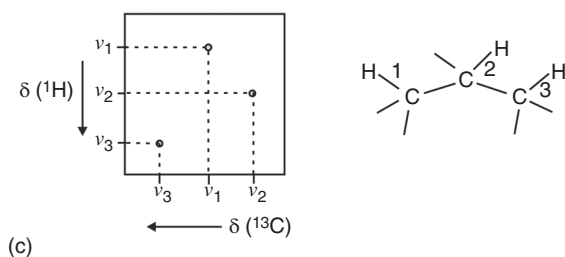
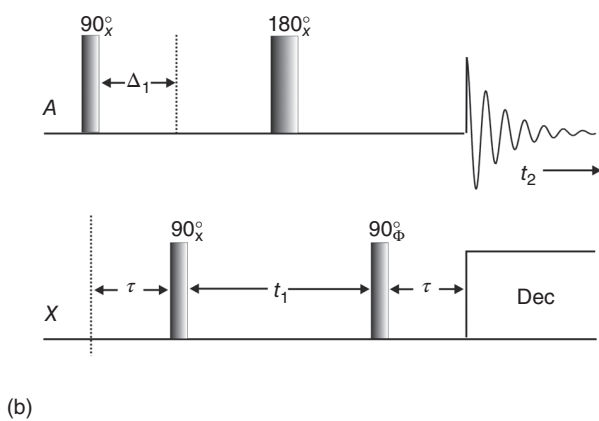
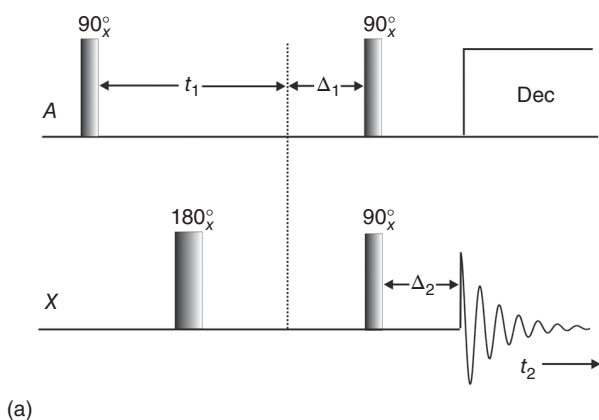


Figure 1.50 A-X HETCOR experiments. (a) Pulse sequence for direct X acquisition and decoupling in both dimensions: $\Delta_1 = 1/(2 \ ^1J_{AX})$ and $\Delta_2 \approx 1/(3 \ ^1J_{AX})$. (b) HMQC pulse sequence for inverse A detection: $\Delta_1 = 1/(2 \ ^1J_{AX})$. (c) Example of 2D spectrum highlighting cross-peaks connecting signals of scalar coupled ^1H and ^{13}C nuclei.

Figure 1.51 NOESY experiment: pulse sequence and example of 2D spectrum highlighting cross-peaks connecting signals of dipolar coupled ^1H nuclei.

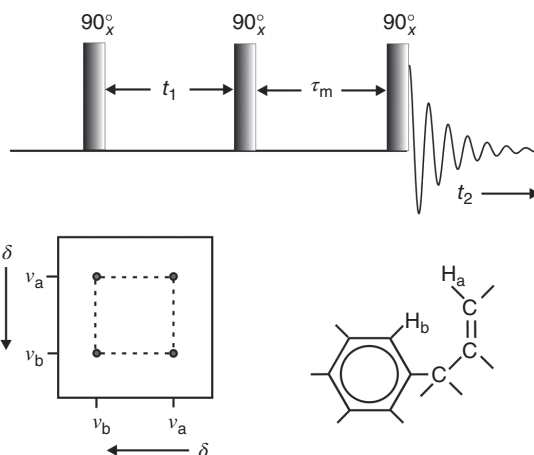
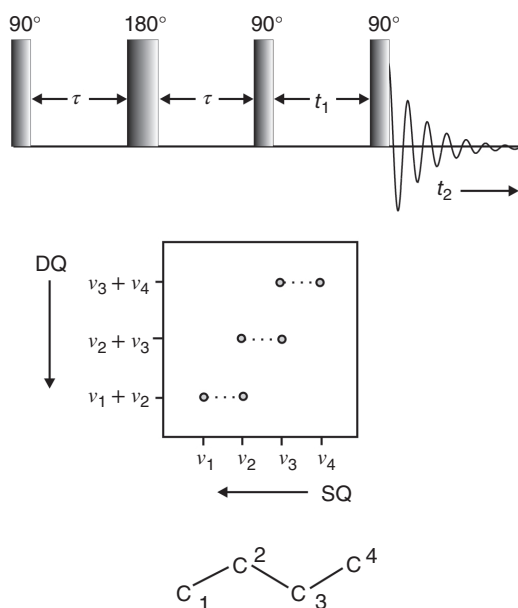


Figure 1.52 INADEQUATE experiment: pulse sequence and example of 2D spectrum highlighting pairs of cross-peaks connecting signals of scalar coupled ^{13}C nuclei.



seen how static lineshapes in solids are strongly affected by exchange among different molecular conformations. Here, we deal with an exchange between two or a few situations corresponding to different conformations or chemical sites (Figure 1.53), which may affect solution-state NMR spectra.

Typical lineshapes for isolated spin-1/2 nuclei, which undergo chemical exchange between two sites A and B, characterized by different resonance frequencies, are depicted in Figure 1.54. Upon increase of the rate constant (i.e. the sample temperature), the NMR lines start to broaden. After the lines merged to a single line, a linewidth reduction is registered upon increase of the rate constant. The point of maximum line broadening is denoted as the “coalescence point,” and it is obtained

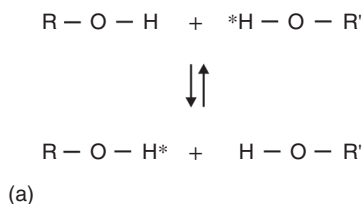


Figure 1.53 Examples of chemical exchange. (a) Nuclei moving between two different molecules through breaking and formation of chemical bonds. (b) Nuclei moving between two different positions in the molecule through interconformational motions.

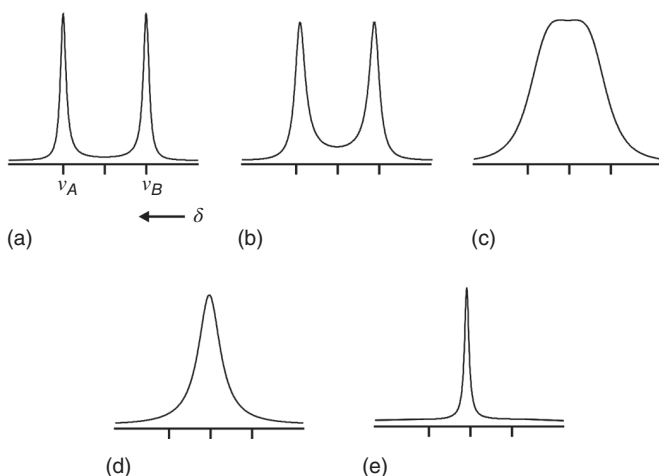
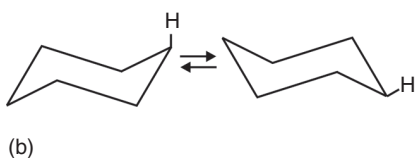


Figure 1.54 Typical lineshapes due to a spin-1/2 exchanging between two different sites at different exchange rates, which increase from (a) to (e). (a) and (b) are in the slow exchanging regime, (c) corresponds to coalescence, and (d) and (e) are in the fast exchanging regime. Note that the vertical scale is not preserved over the different spectra.

when the rate constant k of the exchange process is $\pi/\sqrt{2}$ times the resonance frequency difference $\Delta\nu = |\nu_B - \nu_A|$ of the exchanging sites. Accordingly, the slow motional region is given by $k < \Delta\nu$, while for the fast motional region, $k > \Delta\nu$.

Such dynamic NMR lineshapes can be calculated via modified Bloch equations, which are extended by the kinetic part that accounts for chemical exchange. For a general two-site exchange,



with the complex transverse magnetizations of sites A and B given by $G_i = M_{x,i} + iM_{y,i}$, the equations, obtained by incorporating exchange into the Bloch equations, known

as McConnell equations, are given by

$$\begin{aligned}\frac{dG_A(t)}{dt} &= i(\omega_A - \omega)G_A - \frac{G_A}{T_{2,A}} - k_A G_A + k_B G_B \\ \frac{dG_B(t)}{dt} &= i(\omega_B - \omega)G_B - \frac{G_B}{T_{2,B}} - k_B G_B + k_A G_A\end{aligned}\quad (1.96)$$

where $\omega = \omega_{rf}$ and ω_A and ω_B are the resonance frequencies of *A* and *B*. Equation (1.96) can be solved analytically. The general solution for the NMR lineshape of a degenerate two-site exchange (i.e. identical equilibrium populations of both sites, and $k_A = k_B = k$) case is

$$F(\omega) = C \frac{\tau(\omega_A - \omega_B)^2}{4(\omega - \bar{\omega})^2 + \tau^2(\omega_A - \omega)^2(\omega_B - \omega)^2} \quad (1.97)$$

where it was assumed $T_2 \rightarrow \infty$, C is a proportionality constant, and

$$\bar{\omega} = \frac{1}{2}(\omega_A + \omega_B); \quad \tau = \frac{1}{k} \quad (1.98)$$

In the slow motional region ($k < \Delta\nu$), the dynamic linewidth is found to follow

$$\Delta\nu_{1/2,\text{dyn}} = \frac{1}{\pi\tau} \quad (1.99)$$

which can be understood by a lifetime or uncertainty broadening. In the fast-exchange region ($k > \Delta\nu$), the NMR linewidth is given by

$$\Delta\nu_{1/2,\text{dyn}} = \frac{1}{2}\pi(\nu_A - \nu_B)^2\tau \quad (1.100)$$

At the coalescence point with the maximum linewidth, the equation

$$\frac{1}{\tau} = \frac{\pi(\nu_A - \nu_B)}{\sqrt{2}} \quad (1.101)$$

holds. That is, the coalescence point can be exploited to directly extract the rate, if the chemical shift values of sites *A* and *B* are known. More generally, a best fit of the experimental NMR lineshapes provides the corresponding rate constants from which the kinetic parameters (activation energies, pre-exponential factors) of the underlying process are derived.

It should be emphasized that high-resolution NMR lineshape studies can only be applied for motions that involve changes of the isotropic chemical shifts and/or the scalar spin-spin couplings. For this reason, it is not possible to examine molecular reorientations that do not affect the isotropic magnetic interactions. However, this can be possible by SSNMR methods, as discussed in Chapter 7, as in this case, the anisotropic part of the magnetic interactions is considered.

Finally, very slow motions can be probed by selective excitation or 2D exchange experiments (EXSY – exchange spectroscopy). The latter experiment uses the same pulse sequence as discussed above for the NOESY experiment (Figure 1.55). The difference between EXSY and NOESY experiments is that in the former, the cross-peaks are dominated by chemical exchange effects, while in the latter, relaxation effects

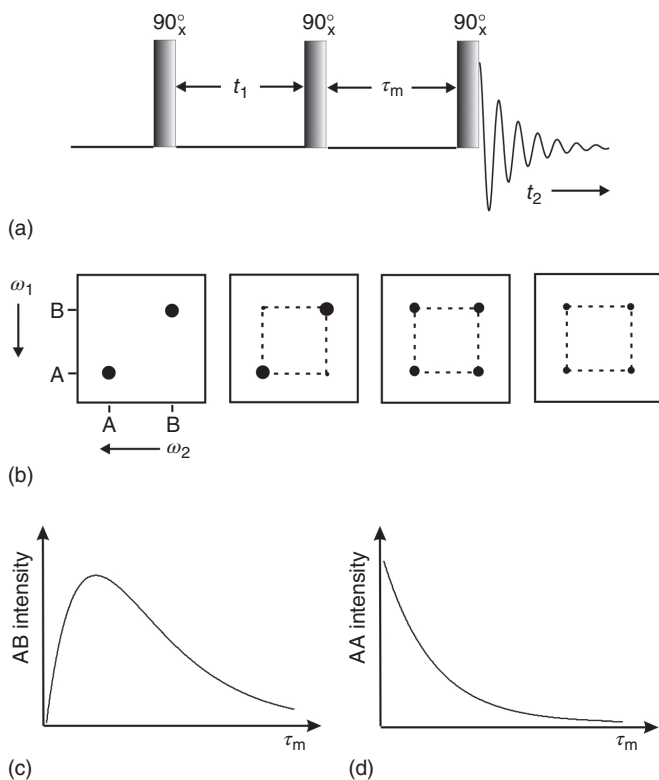


Figure 1.55 Basic EXSY experiment: (a) pulse sequence, (b) example of 2D spectra highlighting the change of the intensity of the diagonal peaks and the cross-peaks connecting signals of exchanging nuclei as a function of τ_m , (c) trend of the intensity of cross-peaks as a function of τ_m , and (d) trend of the intensity of diagonal peaks as a function of τ_m .

have to be considered. From the intensity of the cross-peaks in EXSY spectra as a function of the mixing time τ_m , the exchange rate constants can be obtained. For instance, for a degenerate two-site exchange process the intensities of the diagonal and cross-peaks are

$$a_{\text{diag}}(\tau_m) = C \cdot \exp(-\tau_m/T_1) [1 + \exp(-2k\tau_m)] \quad (1.102)$$

$$a_{\text{cross}}(\tau_m) = C \cdot \exp(-\tau_m/T_1) [1 - \exp(-2k\tau_m)] \quad (1.103)$$

In the limit of short mixing times τ_m , the ratio between the diagonal and cross-peaks can be approximated by

$$\frac{a_{\text{diag}}(\tau_m)}{a_{\text{cross}}(\tau_m)} = \frac{1 + \exp(-2k\tau_m)}{1 - \exp(-2k\tau_m)} \approx \frac{1 - k\tau_m}{k\tau_m} \approx \frac{1}{k\tau_m} \quad (1.104)$$

which allows a direct determination of the rate constant.

1.5 Solid Materials and NMR Spectroscopy

Over the past decades, it has been demonstrated that liquid-state NMR techniques represent a powerful tool for the identification of chemical compounds and structural characterization of unknown substances. Such experiments are performed in an isotropic solution where the studied molecules undergo fast isotropic reorientations, and therefore, only the isotropic parts of the internal nuclear spin interactions – the chemical shift and the scalar spin–spin coupling – remain directly visible. Although they are not directly visible in the NMR spectra, the anisotropic parts of the nuclear spin interactions also play an important role for NMR experiments in isotropic solution, as for spin relaxation phenomena, NOE enhancement, NOESY experiments, etc.

Application of the aforementioned liquid-state NMR methods to solid materials would in general not be very successful. For instance, in solution NMR spectroscopy, only spectral ranges between about 10 ppm = 4 kHz for ^1H (at $B_0 = 9.4\text{ T}$) and 200 ppm = 20 kHz for ^{13}C are typically covered. SSNMR spectra are much broader (up to several hundred kilohertz or even a few megahertz), which is a consequence of the strong, dominant anisotropic (i.e. orientation-dependent) components of the nuclear spin interactions. The signal intensity is much less since it is spread over a large frequency range, and it would therefore be very difficult to detect any signal under typical solution NMR conditions. The anisotropic components of the nuclear spin interactions might be of different origin and depend very much on the particular nuclear spin and the material under investigation. In general, it may be necessary to consider contributions from the following:

- (a) Chemical shift
- (b) Knight shift
- (c) Nuclear quadrupolar interaction
- (d) Homonuclear and heteronuclear direct and indirect spin–spin couplings

Quite often, several nuclear spin interactions are superimposed, which tends to render SSNMR spectra very broad and rather featureless. In Chapter 3, the typical frequency ranges of the abovementioned anisotropic interactions will be discussed in detail. For the moment, it is sufficient to state that the quadrupolar interaction, when present, normally provides the dominant contribution, followed by the dipolar interaction, chemical shift anisotropy and Knight shift, and indirect spin–spin coupling.

Although there is no doubt that liquid-state NMR spectroscopy is a very powerful technique, it is generally not applicable to all substances. For instance, for many substances, there are no suitable solvents available; many substances might be unstable in the dissolved state (i.e. dissociate, disintegrate, etc.) or possess a conformation or structure that is different from the solid state. Moreover, since the bulk or material properties of a substance are directly related to its molecular properties, i.e. the molecular structure and some inherent molecular mobility, it is important and attractive to study a material in its pure state, which quite often is the solid state.

For this reason, even in the early days of NMR spectroscopy, the experiments were not limited to the liquid state. Rather, NMR studies were also performed on solid materials. During the last four decades, SSNMR methods along with the corresponding dedicated hardware have been greatly improved, which nowadays allows SSNMR studies in routine operation. Hardware improvements include the performance and reliability of the spectrometer console, i.e. the complete RF part, power amplifiers, and NMR probes, the development of very fast sample spinning techniques, as well as the increase of the static magnetic field strength. They provided the basis for numerous methodological developments, and nowadays, NMR experiments in the solid state steadily approach the quality, sensitivity, and resolution that is known from solution NMR spectroscopy.

As will be outlined later, there is a great variety of SSNMR techniques available. They have to be chosen based on the particular system under investigation and the questions to be answered. The various experiments and techniques address, for instance, signal-to-noise improvement by magnetization transfer, selective removal, or reintroduction of distinct internal nuclear spin interactions by decoupling/recoupling or sample rotation, etc. In this context, the experimental approach also differs if dilute or abundant spins are considered or if $I = 1/2$ or quadrupolar nuclei are involved. Likewise, it is sometimes advisable to undertake SSNMR studies in broadline mode rather than (or in addition to) under high-resolution conditions, as, for instance, for NMR investigations on dynamics.

In general, SSNMR spectroscopic techniques have to be applied in place of solution-state NMR for all those systems for which – due to the lack of fast isotropic overall motions – anisotropic magnetic interactions still remain to some extent. Questions that can be addressed by such investigations might be related to the structural properties as well as to the motional features in such anisotropic molecular environments.

SSNMR spectroscopy is a nondestructive technique with a great advantage over other techniques used for investigating structural and dynamic properties of solids, which is its general applicability to any type of solid material, either highly ordered, crystalline, or disordered and amorphous or inhomogeneous. In this regard, it is useful to briefly recall the main structural and dynamic characteristics of *crystalline and amorphous and semicrystalline materials*. *Crystalline materials* possess a three-dimensional long-range order with perfectly packed atoms, ions, or molecules. It is interesting to note that molecular mobility can be registered even in highly crystalline solids. This includes high-frequency vibrations of the molecules, which is reflected by a finite Debye–Waller factor in X-ray diffraction and reduced nuclear spin interaction constants in NMR spectroscopy, as well as reorientations of single groups corresponding to jumps among different molecular conformations (phenyl ring flips, methyl reorientations about its ternary symmetry axis, etc.). *Amorphous and semicrystalline materials* are characterized by a high degree of structural disorder, which, in some cases, is associated with chemical heterogeneity. Moreover, they can exhibit considerable internal molecular dynamics. Typical examples of these materials are polymers, glasses, ceramics, or inorganic–organic hybrid systems.

A peculiar class of materials with phase properties somehow intermediate between a crystalline solid and an isotropic liquid is that of liquid crystals. Their features will be briefly described at the end of this section within a short selection of materials to which SSNMR can be successfully applied.

In the following, the main structural and dynamic properties of solid materials that can be characterized by means of SSNMR spectroscopy are briefly presented.

It is taken as read that structural characterizations of solid materials can also be done by means of other experimental techniques. Here, it is necessary to specify the structural information that is required from the experimentalist, i.e. the length scale that should be addressed during the experiment. In general, it is advisable to distinguish between atomic scales (up to a few Å), an intermediate range (up to about 30 Å), and a mesoscopic range (up to about 100–150 Å). Atomic-scale probes comprise X-ray absorption techniques (extended X-ray absorption fine structure [EXAFS], X-ray absorption near edge structure [XANES]), ultraviolet (UV), infrared (IR), and Raman spectroscopy. For the intermediate range X-ray, electron and neutron diffraction techniques can be applied, while the mesoscopic range is accessible by small-angle X-ray scattering (SAXS) and neutron scattering. NMR spectroscopy probes the local environment around the selected nuclei on the atomic scale up to the intermediate range and in some cases can also give structural information on the mesoscopic range. As already said, unlike other techniques – such as X-ray diffraction, which requires crystalline, highly ordered materials – SSNMR spectroscopy is generally applicable. Therefore, it can provide structural information on a variety of compounds with a lack of order and homogeneity, such as polymers, hybrid materials, and glasses, where diffraction studies are hardly applicable. The structural information of the system under investigation is obtained via the size and the modulation of distinct internal nuclear spin interactions – given by the probed nucleus – which in turn determines the length scale probed during the NMR experiment. Hence, the chemical shift anisotropy and quadrupolar interaction examine – via electronic effects – the local neighborhood in a radius of 1–3 Å around the nuclei and provide information about the chemical bonding, coordination sphere, and bonding angles. The same holds for the indirect spin–spin coupling, from which also intramolecular connectivities are obtained. Homonuclear and heteronuclear dipole–dipole interactions are suitable for relatively short interatomic distances, which include intramolecular direct-bond contributions as well as intramolecular and intermolecular through-space contributions. Here, depending on the involved nuclei, the maximum distances are between about 5 and 10 Å (in favorable cases even 15 Å). Even larger distances are accessible through the analysis of spin-diffusion effects and MQ spectra in highly abundant spin systems, providing domain sizes up to 1000 Å. In summary, NMR spectroscopy is a probe for structure determination that is more generally applicable than other techniques, which are also frequently employed on the same length scale. Moreover, although it is clear that structural characterization may require the combination of various experimental techniques, in general, NMR spectroscopy offers the possibility of studying several NMR-active nuclei. For this reason, the use of multinuclear SSNMR spectroscopy for structural characterization

is often superior to other experimental techniques. Finally, it must be said that, even if the majority of SSNMR investigations are performed on *polycrystalline or powder samples* that, as previously described, are in general characterized by broad NMR lineshapes, *single crystals or other oriented materials* (fibers, oriented liquid crystals, etc.) can also be studied. In these cases, NMR spectroscopy can also provide information about the absolute orientation and the degree of alignment in the sample under investigation.

It is important to realize that the structural aspects of a sample cannot be considered completely independently, but have to be discussed in connection with the inherent dynamic behavior of the materials. Hence, structural disorder may arise from *static disorder*, due to a nonuniform static distribution of the structural components, or *dynamic disorder*, due to structural components that are mobile enough to affect the experimental NMR parameters (lineshapes, relaxation data, etc.). This separation is not arbitrary, but is related to the timescales of the involved NMR experiments (see Chapter 7). SSNMR spectroscopy, in general, can distinguish between static and dynamic disorder. It therefore also provides important information about the dynamic features of the sample, which normally also have implications on its bulk (macroscopic) properties. In this regard, SSNMR spectroscopy, exploiting a variety of nuclear properties and experiments, can characterize motional processes (not only reorientations of molecules or molecular groups but also, in specific cases, overall reorientations and collective fluctuations) occurring over a very wide range of characteristic motional times, from picoseconds to seconds (see Chapter 7). Among the techniques able to give dynamic information on solid systems, only dielectric spectroscopy can explore a time range wider than SSNMR. However, while dielectric spectroscopy furnishes information on the dynamics of the whole molecule, resulting from the time dependence of the electric dipolar moment, the exploitation of nuclear probes enables NMR to study motions in a much more detailed and site-specific way.

In the following, we consider an incomplete selection of solid (or, more in general, anisotropic) materials, with very different properties, that can be investigated by means of SSNMR. It should be emphasized that, even if paramagnetic materials can also be investigated, studies on diamagnetic materials are in general preferred. Indeed, the NMR spectra of paramagnetic materials are usually very broad due to the Knight or the paramagnetic interactions, which often prevent detailed information from being obtained. For instance, the Knight shift arising from the conduction electrons, together with the skin effect, makes NMR studies on *metals* normally less attractive.

Organic small molecules and inclusion compounds. Organic small molecules can exist in a variety of crystalline and amorphous solid phases, which can be successfully investigated through SSNMR. Particularly interesting is the application to small organic molecules used in pharmaceuticals, usually as active pharmaceutical ingredients (API). Many API can give rise to different crystalline forms, called polymorphs, depending on many factors (solvent from which they are crystallized, thermal treatment, processing, etc.), as well as to amorphous forms. Often, a simple visual inspection of SSNMR spectra is sufficient for different forms to

be distinguished, therefore allowing a noticeable control over their stability and evolution. This is extremely important in pharmaceuticals since the pharmaceutical behavior of different solid forms is usually different. Moreover, the structural and dynamic properties of the various forms can be characterized in detail. The applicability of SSNMR to amorphous phases makes this technique extremely attractive in this field considering the increasing interest in developing drugs in amorphous forms, which usually exhibit better release properties but worse stability.

Inclusion compounds, which are crystalline guest–host materials with perfectly ordered host structures, are another example of interesting organic solids that can be investigated through SSNMR. The guest species quite often are found to undergo fast bond isomerization and reorientational and even translational motions, which give rise to substantial orientational disorder. At the same time, it has been found that even some host molecules (for instance, urea or thiourea) perform overall reorientational motions that typically occur on a much slower timescale than the aforementioned guest motions.

Synthetic polymers have a semicrystalline or amorphous nature depending on their chemical composition (homopolymers, copolymers), polymerization route (chain branching, etc.), and pretreatment. For instance, semicrystalline polyethylene exhibits crystalline domains with well packed, highly ordered, practically immobile polymer chains and amorphous regions with disordered and entangled chain loops of higher mobility. Amorphous (rubbery or glassy) phases result from chemical heterogeneity in the case of random copolymers or if homopolymers are rapidly quenched from their melt, thus avoiding crystallization. Even polymer melts are normally far from isotropic liquids since the chain mobility is too low to completely average out all anisotropic nuclear spin interactions. Therefore, SSNMR techniques have to be applied for polymer melts as well.

Biopolymers comprise different types of natural polymers such as peptides, proteins, DNA, and polysaccharides. They might be stabilized by a tertiary structure, which provides a high degree of short and long-range order. Nevertheless, there might also be less ordered regions with substantial chain flexibility. Biopolymers might be studied in their pure solid state or – in the case of membrane proteins – embedded in suitable model membranes.

Inorganic glasses again possess chemical and structural heterogeneity, which prevents crystallization. Representative examples are silica or aluminophosphate glasses. Unlike crystalline silica, silica glass exhibits a network with a high degree of structural disorder, as reflected by a distribution of bond lengths and bond angles as well as – in mixed glasses – random distribution of the heteroatoms. Likewise, such glasses possess pores of different sizes, which represent another source of structural heterogeneity. The same structural disorder – as reflected by the random distribution of heteroatoms and variation of bond lengths and angles – also holds for *amorphous ceramics*, such as Si–C–N, Si–C–O, and Si–B–C–N systems. Such materials are, for instance, discussed in connection with surface protection against corrosion or for high-temperature applications. Nevertheless, at sufficiently high temperatures, crystallization takes place accompanied by phase segregations and the formation of *crystalline ceramics* with well-ordered, crystalline domains of

different compositions (for instance silicon carbide or silicon nitride) and with less ordered (amorphous) phase boundaries.

Inorganic–organic hybrid materials cover a large variety of different systems that are the subject of increasing interest because of their unique material properties. Representative examples are intercalates that consist of solid inorganic layers (e.g. clays) and intercalated polymers. Another class of hybrid materials is metal oxides or silica, with modified surfaces through the attachment of alkyl chains or alkyl chain derivatives. The latter materials play an important role, for instance, in chromatography. Metal surfaces with self-assembling monolayers (SAMs), via physisorption of functionalized alkyl chains, and metal-organic frameworks (MOFs), consisting of metal ions or clusters coordinated to organic molecules to form one-, two-, or three-dimensional structures, also belong to the same class of systems. Other inorganic–organic hybrid materials comprise the embedding of small inorganic clusters in a polymer matrix that gives rise to very unusual optical, electrical, and mechanical properties. Such systems are also used as precursor systems for the preparation of ceramic materials. Again, inorganic–organic hybrid materials often show a semicrystalline nature with an immobile (quite often crystalline) inorganic part and an amorphous polymer or organic part, the latter frequently exhibiting pronounced molecular mobility that can be studied by SSNMR. Hybrid biomaterials can also be investigated, where the inorganic part is given by silica, carbonates, phosphates, sulfates, etc. and the organic component consists of polypeptides, proteins, or, more in general, biopolymers. Here, a particular focus is given to the interface between the inorganic part and the biopolymer component.

Zeolites and related porous materials are also an important category of solid materials that can be investigated by SSNMR. A large number of complex zeolite structures are known. They are distinguished by the building units, the size and arrangement of the pores, and the connectivities between the pores. Interesting aspects that can be dealt with by SSNMR comprise (i) the structural evolution during synthesis, (ii) the structural composition of these materials (distribution of SiO_4 and AlO_4 tetrahedra), (iii) the physisorption of organic molecules and their orientation and mobility within the pores (host–guest systems), and (iv) the study of chemical reactions and the role of the zeolite cages and surface.

Plastic crystals are formed by molecules of globular or rodlike shape (for example, fullerene, adamantane, 1,4-diazabicyclo[2.2.2]octane (DABCO), camphor, or nonadecane). Calorimetric studies show solid–solid phase transitions, typically far below the melting point, which are connected with the onset of molecular motions. Hence, in the additional plastic or rotator phases – which can be considered as intermediate phases between the crystalline solid state and the isotropic liquid state – the molecules undergo fast rotations around some molecular symmetry axes, whereas the positional order is maintained. For this reason, X-ray diffraction patterns only exhibit smeared electron densities that are not suitable for structural characterization.

Liquid crystals show intermediate phases (mesophases) between the crystalline state and an isotropic liquid. Liquid crystalline phases are characterized by anisotropic physical properties (birefringence, dielectric permittivity, elastic

properties, etc.) with considerable motional freedom, a substantial degree of local orientational order – defined by the director axis and order parameter(s) – within the liquid crystalline domains, and reduction or loss of positional order, which strongly depends on the actual mesophase. Unlike crystalline solids, in liquid crystalline phases, there is a lack of medium- or long-range ordering. X-ray diffraction data are therefore of limited use. The molecular mobility includes intramolecular motions, overall reorientations, collective fluctuations, and translational motions, which might occur on quite different timescales. It is worth noting that the concept of liquid crystallinity is not restricted to small molecules. Rather, in recent decades, a lot of work has been done in the area of liquid crystalline polymers (main-chain or side-chain systems). Further differentiation is made between thermotropic and lyotropic liquid crystals. In *thermotropic liquid crystals*, the different mesophases are simply obtained by temperature variation. Thermotropic liquid crystalline phases might be found for pure chemical substances with the pronounced anisotropic molecular shape or for mixtures of such compounds, which typically may allow to shift and extend the temperature range of the mesophase. Depending on the chemical structure and sample composition, nematic, various types of higher-ordered smectic and columnar phases can be found that are distinguished by the arrangement of the molecules. Chiral compounds can exhibit cholesteric phases where the orientation of the director axis in the sample follows a screw axis. It is possible to macroscopically align the liquid crystalline domains in nematic phases by strong external magnetic or electric fields. In addition, mechanical forces (e.g. orientation on glass plates) can also be used to achieve domain alignment. *Lyotropic liquid crystalline phases* are formed by amphiphilic molecules in the presence of water (or, rarely, of other solvents). Here again, several types of liquid crystalline phases exist (lamellar phases, hexagonal phases, cubic structures) depending on the structure of the lyotropic molecule, the amount of solvent, and the temperature. Very prominent and important examples are biological membranes, which consist of phospholipid bilayers in which other components, such as cholesterol, peptides, or proteins, are embedded. The chemical composition, water content, and temperature also have a strong impact on physical properties, such as membrane fluidity, stiffness, and permeability. Macroscopic alignment is possible by mechanical forces or, if suitable mixtures are employed (see bicelles), by strong external magnetic fields.

Applications of SSNMR techniques to some of these categories of materials will be presented in Chapter 8.

References

- Aerts, A. and Brown, A. (2019). *J. Chem. Phys.* 150: 224302.
- Andrew, E.R., Bradbury, A., and Eades, R.G. (1959). *Nature* 183: 1802.
- Andrew, E.R. (2007). Andrew, E. Raymond: Spinning the spins: a lifetime in NMR. In: *Encyclopedia of Magnetic Resonance* (eds-in-chief R.K. Harris and R. Wasylshen). Chichester, UK: Wiley <https://doi.org/10.1002/9780470034590.emrhp0009>.

- Becker, D. and Fisk, L. (2007). Development of NMR: from the early beginnings to the early 1990s. In: *Encyclopedia of Magnetic Resonance* (eds-in-chief R.K. Harris and R. Wasylishen). Chichester, UK: Wiley <https://doi.org/10.1002/9780470034590.emrhp0001>.
- Bowers, C.R. and Weitekamp, D.P. (1986). *Phys. Rev. Lett.* 57: 2645.
- Burum, D.P. and Rhim, W.-K. (1979). *J. Chem. Phys.* 71: 944.
- Carr, H.Y. and Purcell, E.M. (1954). *Phys. Rev.* 94: 630.
- Chmelka, B.F., Mueller, K.T., Pines, A. et al. (1989). *Nature* 339: 42.
- Eidmann, G., Savelsberg, R., Blümler, P., and Blümich, B. (1996). *J. Magn. Reson. A* 122: 104.
- Emsley, J.W. and Feeney, J. (1995). *Prog. Nucl. Magn. Reson. Spectrosc.* 28: 1.
- Ernst, R.R. and Anderson, W.A. (1966). *Rev. Sci. Instrum.* 37: 93.
- Frydman, L. and Harwood, J.S. (1995). *J. Am. Chem. Soc.* 117: 5367.
- Gerstein, B.C., Pembleton, R.G., Wilson, R.C., and Ryan, L.M. (1977). *J. Chem. Phys.* 66: 361.
- Goldburg, W.I. and Lee, M. (1963). *Phys. Rev. Lett.* 11: 255.
- Gullion, T. and Schaefer, J. (1989). *J. Magn. Reson.* 81: 196.
- Haeberlen, U. and Waugh, J.S. (1968). *Phys. Rev.* 175: 453.
- Hahn, E.L. (1950). *Phys. Rev.* 80: 580.
- Harris, R.K., Becker, E.D., Cabral de Menezes, S.M. et al. (2001). *Pure Appl. Chem.* 73: 1795.
- Harris, R.K., Becker, E.D., Cabral de Menezes, S.M. et al. (2008). *Pure Appl. Chem.* 80: 59.
- Hartmann, S.R. and Hahn, E.L. (1962). *Phys. Rev.* 128: 2042.
- Hester, R.K., Ackerman, J.L., Neff, B.L., and Waugh, J.S. (1976). *Phys. Rev. Lett.* 36: 1081.
- Kimmich, R. (1980). *Bull. Magn. Reson.* 1: 195.
- Kumar, A., Welti, D., and Ernst, R.R. (1975). *J. Magn. Reson.* 18: 69.
- Lauterbur, P.C. (1973). *Nature* 242: 190.
- Levitt, M.H. and Freeman, R. (1981). *J. Magn. Reson.* 43: 502.
- Llor, A. and Virlet, J. (1988). *Chem. Phys. Lett.* 152: 248.
- Lowe, I.J. (1959). *Phys. Rev. Lett.* 2: 285.
- Mansfield, P. (1970). *Phys. Lett.* 32A: 485.
- Medek, A., Harwood, J.S., and Frydman, L. (1995). *J. Am. Chem. Soc.* 117: 12779.
- Mueller, K.T., Sun, B.Q., Chingas, G.C. et al. (1990). *J. Magn. Reson.* 86: 470.
- Müller, L., Kumar, A., and Ernst, R.R. (1975). *J. Chem. Phys.* 63: 5490.
- Noack, F. (1986). *Prog. Nucl. Magn. Reson. Spectrosc.* 18: 171.
- Pickard, C.J. and Mauri, F. (2001). *Phys. Rev. B* 63: 245101.
- Pines, A., Gibby, M.G., and Waugh, J.S. (1972). *J. Chem. Phys.* 56: 1776.
- Powles, J.G. and Mansfield, P. (1962). *Phys. Lett.* 2A: 58.
- Proctor, W.G. and Yu, F.C. (1950a). *Phys. Rev.* 77: 717.
- Proctor, W.G. and Yu, F.C. (1950b). *Phys. Rev.* 81: 20.
- Purcell, E.M., Pound, R.V., and Bloembergen, N. (1946). *Phys. Rev.* 70: 986.
- Pykkö, P. (2018). *Mol. Phys.* 116: 1328.
- Rabi, I.I., Zacharias, J.R., Millman, S. et al. (1938). *Phys. Rev.* 53: 318.
- Rankin, A.G.M., Truscott, J., Poupoint, F. et al. (2019). *Solid State NMR* 101: 116.

- Rhim, W.-K., Elleman, D.D., and Vaughan, R.W. (1973). *J. Chem. Phys.* 58: 1772.
- Sakellariou, D., Goff, G.L., and Jacquinet, J.-F. (2007). *Nature* 447: 694.
- Samoson, A., Lippmaa, E., and Pines, A. (1988). *Mol. Phys.* 65: 1013.
- Samoson, A., Tuherm, T., Past, J. et al. (2005). *Top. Curr. Chem.* 246: 15.
- Schaefer, J. and Stejskal, E.O. (1976). *J. Am. Chem. Soc.* 98: 1031.
- Schmidt, C., Wefing, S., Blümich, B., and Spiess, H.W. (1986). *Chem. Phys. Lett.* 130: 84.
- Stejskal, E.O. and Tanner, J.E. (1965). *J. Chem. Phys.* 42: 288.
- Waugh, J.S., Huber, L.M., and Haeberlen, U. (1968). *Phys. Rev. Lett.* 20: 180.

